Transient and steady shear rheology of particle-laden viscoelastic suspensions

Anika Jain, and Eric S. G. Shaqfeh

Citation: Journal of Rheology **65**, 1269 (2021); doi: 10.1122/8.0000265
View online: https://doi.org/10.1122/8.0000265
View Table of Contents: https://sor.scitation.org/toc/jor/65/6
Published by the The Society of Rheology

Transient and steady shear rheology of particle-laden viscoelastic suspensions

Anika Jain[1,a)] and Eric S. G. Shaqfeh[1,2,b)]

[1]*Department of Chemical Engineering, Stanford University, Stanford, California 94305*
[2]*Department of Mechanical Engineering, Stanford University, Stanford, California 94305*

(Received 26 February 2021; final revision received 1 August 2021; published 15 September 2021)

Abstract

We study the transient and steady shear rheology of rigid particle suspensions in Boger fluids via complete 3D numerical simulations and experiments. We calculate the transient per-particle extra viscosity and primary stress coefficients for suspensions at different particle volume fractions ϕ for a range of Weissenberg numbers (Wi). The per-particle viscosity (η^p) and the primary normal coefficient (ψ_1^p) increase monotonically to steady state in body-fitted (BF) simulations (for dilute suspensions) and immersed boundary (IB) simulations (for nondilute suspensions). We also present experimental measurements including small amplitude oscillatory shear, steady shear, and transient shear measurements at different particle volume fraction suspensions in a Boger fluid. The simulations and experiments suggest that longer strains are needed to achieve steady state at higher ϕ and Wi. We also show the comparison of the BF and the IB simulations with experimental data for the per-particle viscosity and find excellent quantitative agreement between simulations and experiments at Wi = 3 but the IB simulations underpredict the steady values at higher Wi = 6. Nevertheless, the IB simulations show an increase in the per-particle viscosity with ϕ as witnessed in the experiments. To understand this behavior, we examine the particle-induced fluid stress (PIFS) and the stresslet contributions using a novel method developed for the IB simulations in this work. We find that the PIFS is independent of ϕ but the stresslet values increase with ϕ. Thus, the particle-particle hydrodynamic interactions in nondilute suspensions affect the stresslet and, in turn, the per-particle viscosity at a given Wi. https://doi.org/10.1122/8.0000265

I. INTRODUCTION

The rheology of suspensions of rigid particles in polymeric fluids is a particularly important field of study as these materials find applications in a variety of industries like foods, pharmaceuticals, adhesives and coatings, paints, personal care products, and biomedical devices. Moreover, the rheology of these materials can be complex when compared to suspensions in Newtonian fluids. In this context, noncolloidal suspensions of rigid particles in Newtonian fluids exhibit no shear rate dependence in steady shear flow for particle volume fractions ϕ less than 30% [1,2], but this is not the case when the suspending fluid is polymeric. In the present article, we will focus on suspensions in the so-called "Boger fluids" [3], as we are interested in understanding how the fluid elasticity affects the flows of rigid particle suspensions. Boger fluids are highly elastic fluids that exhibit nearly constant viscosity for a range of shear rates [3–5]. Previous experimental studies show that noncolloidal suspensions in Boger fluids exhibit shear-thickening behavior in steady shear flow, for all particle volume fractions down to 5% [4,5]. The response of rigid particle suspensions in such viscoelastic fluids has been shown to be nonlinear in shear rate because of complex particle-fluid interactions as well as hydrodynamic interactions between particles even at $\phi \leq 10\%$ [5–7]. Previously, noncolloidal suspensions in viscoelastic fluids have been studied in steady shear flows mostly through experiments for relatively concentrated suspensions [4,8,9], but there are very few computational simulation studies in the literature that may shed light on these experiments. The two-dimensional (2D) simulations of suspensions by Hwang *et al.* [10] using an Oldroyd-B model matrix have been instructive, but for three-dimensional (3D) simulations, there are only the works of Hwang *et al.* [11], D'Avino *et al.* [12], Yang *et al.* [5,13], and Vázquez-Quesada *et al.* [7].

Yang *et al.* [13] performed complete 3D numerical simulations of dilute suspensions in steady shear flow where the authors computed the per-particle "extra" viscosity contribution to the suspension viscosity as a function of Weissenberg number (Wi). They found that the per-particle viscosity increases with Wi and plateaus at large values of Wi. The authors performed numerical calculation of the two extra stress contributions that come from the addition of rigid particles to the nonlinear elastic fluid: (1) the particle-induced fluid stress (PIFS), which is a measure of extra stress in the fluid phase due to the presence of particles, and (2) the particle stresslet, which is a measure of stress in the particle region as rigid particles resist deformation. The authors of the same study found that the increase in per-particle viscosity was caused by an increase in PIFS with the Wi. In a subsequent study [6], they looked into the mechanism of thickening via the PIFS by analyzing the flow type in the regions of significant polymer-induced fluid stress and found that the stretch of polymers in strain-dominated flow within closed streamlines around the particles generates large stresses that contribute to the thickening behavior. We refer the readers to the article for further details.

[a)]Author to whom correspondence should be addressed; electronic mail: anikaj@stanford.edu
[b)]Electronic mail: esgs@stanford.edu

Numerical simulations studies of multiple-particle systems include the recent work of Yang and Shaqfeh [5] who studied the steady shear rheology of noncolloidal, nondilute suspensions in Boger fluids via numerical simulations using a 3D, finite-volume method. The authors in the study used an immersed boundary (IB) method to simulate an ensemble of particles as a function of time until they achieved steady average bulk properties. They showed that the viscosity of suspensions with particle volume fraction $\phi \leq 10\%$ in numerical simulations can be characterized by a shift factor that depends on the zero shear viscosity and suggested a "master" curve that describes the viscosity thickening for all ϕ values. The master curve could be determined by single-particle-fluid interactions only and is apparently not dependent on particle-particle interactions when plotted as a function of the suspension stress. The authors demonstrated that the master curve exists for the thickening of the shear viscosity not only in simulations but also in their experimental data and other experimental data in the literature. Numerical simulations underpredicted the master curve.

In another recent publication, Vázquez *et al.* [7] performed 3D numerical simulations using the smoothed particle hydrodynamics method to study the rheology of noncolloidal suspensions of rigid spherical particles in a viscoelastic matrix. They reported that they needed to perform full many-particle simulations with no *a priori* specification of their spatial distribution to recover precisely experimental values even under dilute conditions. They found that the agreement was quantitative between multiple-particle simulations and experiments for particle volume fraction $\phi = 5\%$ but qualitative only for $\phi = 10\%$ and 30% as the simulations underpredicted the experimental viscosity measurements of suspensions.

In this work, we study the time-dependent evolution and steady values of the bulk shear stress in rigid particle suspensions during start-up of shear flow via experiments and numerical simulations. The suspensions are composed of spherical particles suspended in Boger fluids. Note that the time dependent response of viscoelastic suspensions is of great practical and fundamental importance because, typically, it takes 10–100 shear strain for these materials to reach steady state in the start-up of shear flow, and it is often difficult to achieve such high strains in practical situations. We are not aware of any theoretical or 3D direct numerical studies that compute the viscometric functions or any experimental data of viscoelastic suspensions undergoing start-up of shear flow appearing in any previous work. In this study, we perform time-dependent complete 3D simulations in the dilute limit (i.e., single particle) using a body-fitted (BF) code [13] and in the nondilute limit using an immersed body method [14,15]. We also present transient shear experiments of suspensions in a Boger fluid at different particle volume fractions, $\phi \leq 20\%$. The focus is on low volume fraction suspensions where the bulk properties are dominated by long range hydrodynamic interactions rather than close range "lubrication" or "collisional" particle-particle interactions. We directly compare our experiments and numerical simulations to assess their agreement and to understand the observed rheological behavior in experiments with the help of numerical tools. Thus, the aim is to determine how the time-dependent rheology of particle suspensions differs from the suspending Boger fluid in the start-up of shear flow within a range of particle loadings at multiple shear rates.

This paper is organized as follows. In Sec. II, we describe numerical methods used to perform the transient shear simulations of suspensions in viscoelastic fluids. Next, the numerical results from the BF simulations are validated by comparing to a transient small Wi theory developed in this work. Thereafter, we validate the IB simulations by comparing with the converged BF simulations. We describe a novel method of calculating the stresslet and PIFS in IB simulations where the particle interface does not have to be defined. This also includes a new approach to calculate the first normal stress difference coefficient in IB simulations. In Sec. III, we present the numerical results of the BF simulations for dilute particle suspensions in a Boger fluid considered by Dai *et al.* [4] over the range $0.3 \leq \mathrm{Wi} \leq 4$. Next, we present BF and IB simulation results for particle suspensions in a Boger fluid that we prepared in the laboratory (referred to as B25 fluid in this study) at two values of $\mathrm{Wi} = 3$ and 6. In Sec. IV, we report a set of laboratory experiments for the characterization of the B25 Boger fluid and the associated suspensions with different ϕ ranging from 2.5% to 20%. The measurements include small amplitude oscillatory shear (SAOS), steady shear, and transient shear experiments of the B25 Boger fluid and the suspensions. In Sec. V, we show the comparison of the per-particle viscosity and the primary normal stress coefficient from experiments and numerical simulations in transient shear flow at $\mathrm{Wi} = 3$ and 6. In Sec. VI, we examine the mechanism of the increase in per-particle viscosity with ϕ at a given Wi observed in both experiments and IB simulations by performing the decomposition of the per-particle viscosity into PIFS and stresslet contributions to determine how these components change with ϕ. We also determine if there is a need to perform multiple-particle simulations or if it suffices to do single-particle simulations to study the shear rheology of $\phi \leq 10\%$ suspensions. In Sec. VII, we summarize the main findings.

II. PROBLEM FORMULATION

A. Bulk rheology of a suspension

We first summarize the calculation of the appropriate viscometric functions in our numerical simulations, the details of which are given in studies by Yang and Shaqfeh [5,6]. To obtain the bulk stress in a suspension of freely suspended, noncolloidal spheres in a viscoelastic fluid, we need to ensemble average over many configurations of the suspension. Equivalently, we can average over a sufficiently large volume of the suspension (large compared to interparticle distance assuming "reasonable randomness" [16]) where the mean velocity is specified to be a shear flow $\langle u_i \rangle = \dot{\gamma} x_2 \delta_{i1}$. The angle bracket denotes a spatial average over the volume V. We have the following expression for the bulk stress of the suspension:

$$\langle \sigma_{ij} \rangle = \frac{1}{V} \int_V \sigma_{ij} \mathrm{d}V \tag{1}$$

or

$$\langle \sigma_{ij} \rangle = \frac{1}{V}\left(\int_{V_f} \sigma_{ij}^{f} \mathrm{d}V + \int_{V_p} \sigma_{ij}^{p} \mathrm{d}V \right), \tag{2}$$

where σ_{ij} is the stress in the suspension that is a function of position and time, V_f is the fluid domain, V_p is the particle domain, σ_{ij}^{f} and σ_{ij}^{p} are the stresses in the fluid phase and particle phase, respectively, and $V = V_f + V_p$. As shown by Yang *et al.* [13], we can split the bulk stress into two contributions—the stress in the suspending fluid in the absence of particles and the "extra" stress due to particles in suspension. The stress due to particles can be further split into PIFS (represented by Σ_{ij} in this study) and stresslet (represented by S_{ij} in this study) as

$$\langle \sigma_{ij} \rangle = \sigma_{ij}^{f0} + n\left(\Sigma_{ij} + S_{ij}\right), \tag{3}$$

where σ_{ij}^{f0} is the fluid stress in the absence of particles. This can be computed analytically for the Oldroyd-B model and numerically for the Giesekus model.

After we apply the divergence theorem to write the volume integral over the particle domain as a surface integral in Eq. (2) (assuming freely suspended particles), we can calculate the PIFS and stresslet using local stress values as

$$\Sigma_{ij} = \frac{1}{N}\int_{V} (\sigma_{ij}^{f} - \sigma_{ij}^{f0}) \mathrm{d}V, \tag{4}$$

$$S_{ij} = \frac{1}{N}\int_{A_p} x_j \sigma_{ik}^{f} n_k \mathrm{d}A, \tag{5}$$

where N is the number of particles in the system and $n = N/V$ is the number density; A_p is the surface of all particles and x_j is a position vector on the surface of the particle. For very dilute suspensions, the PIFS and the stresslet can be calculated by considering a subregion of the suspension that contains only a single particle and the disturbances in the flow due to that particle; thus, all interactions are neglected. For these calculations, we use a BF mesh method [13,17,18] where a single stationary mesh that conforms to surface of a single sphere is used. For nondilute suspensions, we need to consider a subregion that contains enough particles to reproduce the bulk behavior. We calculate the bulk viscometric functions in multiple-particle simulations using the same Eq. (3), but it is not possible to use Eqs. (4) and (5) in IB because the particle surface boundary is diffuse in the IB method. Thus, we develop a novel method to calculate the PIFS and stresslet in IB simulations in Sec. II C. The material functions of primary interest are the suspension shear viscosity and first normal stress coefficient and in dimensional form they are given by the equations

$$\eta = \frac{\sigma_{12}^{f0}}{\dot{\gamma}} + n\frac{\Sigma_{12} + S_{12}}{\dot{\gamma}}, \tag{6}$$

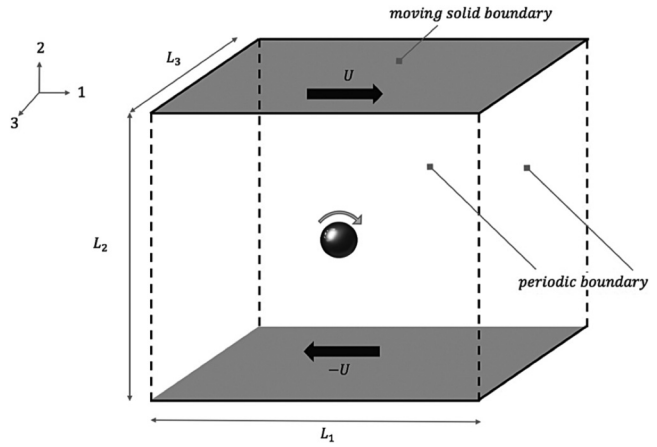

FIG. 1. Schematic of a sphere placed at the center of computation domain in shear flow. This image is taken from Yang *et al.* [13].

$$\psi_1 = \frac{\sigma_{11}^{f0} - \sigma_{22}^{f0}}{\dot{\gamma}^2} + n\frac{\Sigma_{11} - \Sigma_{22} + S_{11} - S_{22}}{\dot{\gamma}^2}. \tag{7}$$

B. Governing equations

For modeling dilute suspensions, we consider a neutrally buoyant sphere placed at the center of a rectangular computation domain $(\pm L_1/2,\ \pm L_2/2,\ \pm L_3/2)$ in a mean flow field $\langle u_i \rangle = \dot{\gamma} x_2 \delta_{i1}$ where $\dot{\gamma}$ is the shear rate. The schematic of the single sphere BF simulation geometry is shown in Fig. 1. For nondilute suspensions, we employ IB simulations; thus we consider N spheres, each of radius a, that are freely suspended in a computation domain shown in Fig. 2. The linear velocity and angular velocity of the spheres in both cases are updated at each time step such that they are force free and torque free at all times in the applied shear flow. The mean flow is imposed on the walls of the domain $u_i = (\pm \dot{\gamma} L_2/2, 0, 0)$ at $x_2 = \pm L_2/2$, and the boundaries at

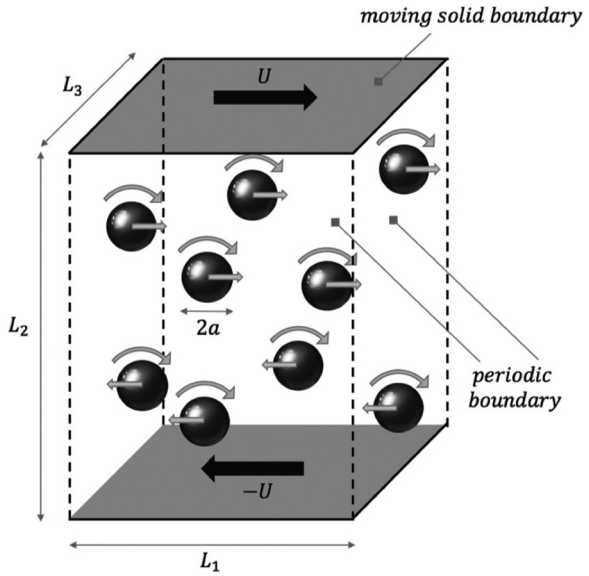

FIG. 2. Initial random distribution of spheres in a computational box for IB simulations. This image is taken from Yang and Shaqfeh [5].

$x_1 = \pm L_1/2$ and $x_3 = \pm L_3/2$ are periodic. The governing equations for the simulation of fluid flow around rigid particles are the continuity and momentum balance equations shown below, suitably made dimensionless,

$$\frac{\partial u_i'}{\partial x_i'} = 0; \quad Re\left(\frac{\partial u_i'}{\partial t'} + u_j'\frac{\partial u_i'}{\partial x_j'}\right) = -\frac{\partial p'}{\partial x_i'} + \frac{\partial \sigma_{ij}^{f'}}{\partial x_j'}, \tag{8}$$

where prime denotes a nondimensional variable. Length is made dimensionless by the particle radius a, time by inverse shear rate $\dot{\gamma}$, velocity by $\dot{\gamma}a$, and stress by $\eta_0\dot{\gamma}$, where η_0 is the zero shear viscosity of the suspending fluid. The Reynolds number is defined as $Re = \rho\dot{\gamma}a^2/\eta_0$. The fluid stress $\sigma_{ij}^{f'}$ in Eq. (8) is the sum of Newtonian and polymer stress,

$$\sigma_{ij}^{f'} = \beta\left(\frac{\partial u_i'}{\partial x_j'} + \frac{\partial u_j'}{\partial x_i'}\right) + \tau_{ij}^{p'}, \tag{9}$$

where $\beta = \eta_s/\eta_0$ is the ratio of Newtonian solvent viscosity to the zero shear viscosity of the suspending fluid and $\tau_{ij}^{p'}$ is the nondimensional polymer stress. We use the Oldroyd-B and the Giesekus models for the suspending Boger fluids used in this work. The Oldroyd-B equation describing the evolution of the polymer conformation tensor C_{ij} in a flow field is

$$\frac{\partial C_{ij}}{\partial t'} + u_k'\frac{\partial C_{ij}}{\partial x_k'} - C_{ik}\frac{\partial u_j'}{\partial x_k'} - C_{jk}\frac{\partial u_i'}{\partial x_k'} = -\frac{\tau_{ij}^{p'}}{1-\beta}, \tag{10}$$

and the Giesekus model equation is given by

$$\frac{\partial C_{ij}}{\partial t'} + u_k'\frac{\partial C_{ij}}{\partial x_k'} - C_{ik}\frac{\partial u_j'}{\partial x_k'} - C_{jk}\frac{\partial u_i'}{\partial x_k'} = -\frac{\tau_{ij}^{p'}}{1-\beta} - \frac{\alpha}{Wi}(C_{ik}-\delta_{ik})(C_{kj}-\delta_{kj}), \tag{11}$$

where the conformation tensor components C_{ij} are nondimensionalized by the polymer radius of gyration squared and α is the mobility parameter. When $\alpha = 0$, the Giesekus equation is equivalent to the Oldroyd-B model. The polymer stress is related to the polymer conformation tensor for both Oldroyd-B and Giesekus models through the relation

$$\tau_{ij}^{p'} = \frac{1-\beta}{Wi}\left(C_{ij} - \delta_{ij}\right). \tag{12}$$

The dimensionless groups in Eqs. (11) and (12) are (a) Weissenberg number $\mathrm{Wi} = \lambda\dot{\gamma}$ that is defined as the product of the longest relaxation time of the fluid λ and the imposed shear rate $\dot{\gamma}$ and (b) viscosity ratio $\beta = \frac{\eta_s}{\eta_s+\eta_p}$, where η_p is the polymer viscosity. For completion of the time dependent shear problem, we also require initial conditions for the velocity and conformation tensor. For the initial velocity, we choose the known Newtonian creeping flow solution for shear flow past a single sphere in the dilute limit and solve for the Newtonian flow field for multiple particles using the IB method in the nondilute case. For the initial conformation tensor, it is set equal to the identity tensor (the dimensionless, equilibrium configuration thus producing no polymer stress). We drop primes in rest of the paper for convenience, and all the variables are assumed to be nondimensional.

C. Simulation method

We perform BF simulations for single spheres in a fixed reference frame since by symmetry the sphere does not move even though it is force free. Therefore, the underlying mesh is fixed. The details of BF simulations can be found in Yang *et al.* [13] where the authors used a finite-volume solver to obtain the velocity and stress fields in the fluid domain. We employ the same solver in this work to study the time-dependent evolution of bulk stress in a dilute suspension. We perform a surface integral to compute the stresslet according to Eq. (5) and a volume integral to compute PIFS according to Eq. (4) in the BF simulations. However, we do not perform BF simulations to simulate many moving particles in this computational domain but instead use an implementation based on the class of IB methods [15,19] to simulate multiple particles. In this method, the domain grid does not conform to the particles but covers the entire computation volume, including particle regions. The particles are defined on a separate Lagrangian mesh that is free to translate over the underlying Eulerian mesh domain. The governing equations of flow are solved on the Eulerian mesh including the particle regions. However, an additional volumetric body term f_i' is added to the momentum equation to force the regions on the Eulerian mesh that underlie the Lagrangian particle mesh to move as rigid bodies. The momentum equation for the IB method is shown below,

$$Re\left(\frac{\partial u_i}{\partial t} + u_j\frac{\partial u_i}{\partial x_j}\right) = -\frac{\partial p}{\partial x_i} + \frac{\partial \sigma_{ij}^{f}}{\partial x_j} + f_i. \tag{13}$$

The details of the solver and algorithm that we use as well as the validation tests are described in the paper by Krishnan *et al.* [15]. The IB method has a main disadvantage—the loss of resolution near the particle boundaries due to interpolation of information between the Lagrangian and Eulerian meshes—consequently, the solid-fluid interface is not sharp. The region at the interface is neither fully particle nor fully fluid, and this transition is on the order of the Eulerian mesh size. This is particularly troublesome for calculations of viscoelastic fluids because large polymer stress gradients often occur near the particle surfaces, and the loss of spatial resolution from the IB method can lead to inaccurate stress calculations. This error can be reduced by increasing the Eulerian mesh resolution, but a refinement by a factor of 2 leads to an increase in the computation time by a factor of 16 if we keep the same value of the viscous CFL number. Thus, we have limitations on the number of mesh elements in the computation domain for a given maximum computational time, and this constrains the Wi and the number of particles we can simulate.

Another consequence of a "smoothed" solid-fluid interface is that we need a new method to calculate S_{ij} and Σ_{ij}. The stresslet as defined in Eq. (5) is a surface integral that requires identifying the particle surface and evaluating the fluid stresses at that surface. Since the solid-fluid interface is not sharp, defining a boundary and determining fluid stress on that boundary is not straightforward. A similar issue arises when trying to compute PIFS, Σ_{ij}, which requires assigning each control volume in the domain as fluid or particle, which is not straightforward for the smoothed particle-fluid interface. To address the above issue for IB simulations, Yang and Shaqfeh [5] developed a method to calculate PIFS and stresslet that involved defining the particle surface such that an equality was satisfied between the bulk shear stress and the shear stress on the wall averaged over time,

$$\frac{\langle F_1\rangle}{A} = \sigma_{12}^{f0} + \frac{1}{V}\left\langle \int_V \left(\sigma_{12}^{f} - \sigma_{12}^{f0}\right) \mathrm{d}V \right\rangle + \frac{1}{V}\left\langle \int_{\partial P_1 + \cdots + \partial P_N} \left(x_2 - R_2^n\right)\sigma_{1k}^{f} n_k \mathrm{d}A \right\rangle, \tag{14}$$

where A is the top plate or bottom plate area. In this way, the authors chose the particle surfaces $\partial P_1, \ldots, \partial P_N$ that allowed them to calculate stresslet and PIFS in IB simulations. We use a different and more direct approach in this work that does not require finding the particle surface. We relate the forces on the walls of the computation domain containing particles to the volume averaged stress in the domain by following a similar procedure as shown in Appendix A in Yang *et al.* [13]. We first consider a force balance on an arbitrary domain D, as shown in Fig. 3, where the surface S can be positioned anywhere between the top and bottom walls. The momentum balance in the fluid phase for Stokes flow is

$$0 = -\frac{\partial p}{\partial x_i} + \frac{\partial \sigma_{ij}^{f}}{\partial x_j} + f_i, \tag{15}$$

where f_i is the IB method force density. We consider the volume integral of Eq. (15) over the volume D and apply the divergence theorem

$$\int_D \left(-\frac{\partial p}{\partial x_i} + \frac{\partial \sigma_{ij}^{f}}{\partial x_j} + f_i\right)\mathrm{d}V = 0 \tag{16}$$

$$\int_{\partial D}\left(-p\delta_{ij} + \sigma_{ij}^{f}\right) n_j \mathrm{d}A + \int_D f_i \mathrm{d}V = 0. \tag{17}$$

Because the boundaries are periodic in the vorticity and flow directions, the only surfaces that contribute to the surface integral are the top plate and the surface S,

$$-\int_{Top} p\delta_{i2}\mathrm{d}A + \int_S p\delta_{i2}\mathrm{d}A + \int_{Top}\sigma_{ij}^{f}\delta_{j2}\mathrm{d}A - \int_S \sigma_{ij}^{f}\delta_{j2}\mathrm{d}A + \int_D f_i \mathrm{d}V, \tag{18}$$

Since the position of S is arbitrary, we repeat over N volumes separated by Δx_2 where surface $S(x_2)$ spans from $-L_2/2$ to $L_2/2$ and then multiply by Δx_2. We take the limit $N \to \infty$, $\Delta x \to 0$ and add the results together. For $i = 1$,

$$N\int_{Top}\sigma_{12}^{f}\mathrm{d}A = \frac{1}{\Delta x_2}\int_{-L_2/2}^{L_2/2}\left[\int_S \sigma_{12}^{f}\mathrm{d}A\right]\mathrm{d}x_2 - \frac{1}{\Delta x_2}\int\int\left[\int_{-L_2/2}^{L_2/2}\mathrm{d}x_2\int_{x_2}^{L_2/2} f_1(\sigma, x_1, x_3)\mathrm{d}\sigma\right]\mathrm{d}x_1\mathrm{d}x_3, \tag{19}$$

and changing the limits of integration,

$$\int_{-L_2/2}^{L_2/2}\mathrm{d}x_2\int_{x_2}^{L_2/2}\mathrm{d}\sigma = \int_{-L_2/2}^{L_2/2}\mathrm{d}\sigma\int_{-L_2/2}^{\sigma}\mathrm{d}x_2, \tag{20}$$

with the knowledge $\int_V f_1 \mathrm{d}V = 0$ for freely suspended particles, then we obtain

$$\frac{F_1}{A} = \langle\sigma_{12}^{f}\rangle - \langle x_2 f_1\rangle, \tag{21}$$

where $\langle\cdot\rangle = \frac{1}{V}\int_V(\cdot)\mathrm{d}V$ is the volume averaged quantity and

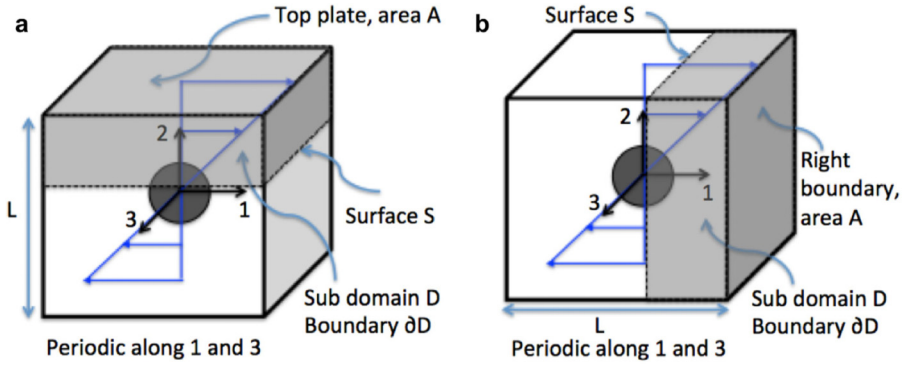

FIG. 3. Schematic showing the (a) force balance that relates force on top plate to bulk stress in domain and the (b) force balance that relates pressure to the thrust on the plane in flow direction. This schematic is taken from Yang *et al.* [13].

$F_1 = \int_{Top} \sigma^f_{12} \mathrm{d}A$. It follows that

$$S_{12} = \left(\frac{F_1}{A} - \langle \sigma^f_{12} \rangle\right)/\phi, \tag{22a}$$

$$S_{12} = -\langle x_2 f_1 \rangle/\phi. \tag{22b}$$

We can compute the stresslet using either Eq. (22a) or Eq. (22b), and the PIFS using the equation below, viz,

$$\Sigma_{12} = \left(\langle \sigma^f_{12} \rangle - \sigma^{f0}_{12}\right)/\phi. \tag{23}$$

Thus, we can compute per-particle viscosity from the sum of the stresslet and the PIFS as

$$\eta^p = \frac{1}{\phi}\left(\frac{F_1}{A} - \langle \sigma^f_{12} \rangle + \langle \sigma^f_{12} \rangle - \sigma^{f0}_{12}\right), \tag{24a}$$

$$\eta^p = \frac{1}{\phi}\left(-\langle x_2 f_1 \rangle + \langle \sigma^f_{12} \rangle - \sigma^{f0}_{12}\right). \tag{24b}$$

Neither Eqs. (22a) and (22b) nor Eq. (23) require knowledge of the position of the particle surface. We only need to compute volume averages over the Eulerian domain and the force on the top plate. For the calculation of N_1 in IB simulations, we can use a similar procedure. If we pick $i = 2$ in Eq. (18) and follow the same averaging procedure, then we obtain

$$\frac{\int_A (\sigma_{22} - p)\mathrm{d}A}{A} = -\langle p \rangle + \langle \sigma^f_{22} \rangle - \langle x_2 f_2 \rangle. \tag{25}$$

The normal force depends on $\langle p \rangle$, which is determined by the conditions applied at the periodic positions. We go back to Eq. (16) with the integral over the volume as shown in Fig. 3 and then we apply the divergence theorem with surface integrals over right periodic zone and S,

$$0 = -\int_{A_{Right}} p\delta_{i1}\mathrm{d}A + \int_S p\delta_{i1}\mathrm{d}A + \int_{A_{Right}} \sigma^f_{ij}\delta_{j1}\mathrm{d}A - \int_S \sigma^f_{ij}\delta_{j1}\mathrm{d}A + \int f_i \mathrm{d}V. \tag{26}$$

Picking $i = 1$ yields

$$0 = -\int_{A_{Right}} p\mathrm{d}A + \int_S p\mathrm{d}A + \int_{A_{Right}} \sigma^f_{11}\mathrm{d}A - \int_S \sigma^f_{11}\mathrm{d}A + \int f_1 \mathrm{d}V, \tag{27}$$

$$\int_{A_{Right}} (\sigma^f_{11} - p)\mathrm{d}A = \int_S (\sigma^f_{11} - p)\mathrm{d}A - \int f_1 \mathrm{d}V. \tag{28}$$

Since the position of surface S is arbitrary, we average over positions of surface S and get

$$\frac{1}{A_{Right}}\int_{A_{Right}} (\sigma^f_{11} - p)\mathrm{d}A = \langle \sigma^f_{11} - p \rangle - \langle x_1 f_1 \rangle. \tag{29}$$

We thus obtain $\langle p \rangle$ from Eq. (29),

$$\langle p \rangle = \langle \sigma^f_{11} \rangle - \langle x_1 f_1 \rangle - \frac{1}{A_{Right}}\int_{A_{Right}} (\sigma^f_{11} - p)\mathrm{d}A. \tag{30}$$

We substitute the above equation for $\langle p \rangle$ in Eq. (25),

$$\frac{1}{A_{Right}}\int_{A_{Right}} (\sigma^f_{11} - p)\mathrm{d}A - \frac{1}{A}\int_A (\sigma^f_{22} - p)\mathrm{d}A = \langle \sigma^f_{11} \rangle - \langle \sigma^f_{22} \rangle - \langle x_1 f_1 \rangle + \langle x_2 f_2 \rangle. \tag{31}$$

The left-hand side or right-hand side (rhs) in the above equation is a measure of the first normal stress difference of the suspension, N_1, in IB simulations. The per-particle contribution to the first normal stress coefficient of suspension is thus calculated using the equation

$$\psi^p_1 = \frac{1}{\phi}\left(\frac{\langle \sigma^f_{11} - \sigma^{f0}_{11} \rangle - \langle \sigma^f_{22} - \sigma^{f0}_{22} \rangle - \langle x_1 f_1 \rangle + \langle x_2 f_2 \rangle}{Wi}\right), \tag{32}$$

where the PIFS contribution is obtained as

$$\frac{\Sigma_{11-22}}{Wi} = \frac{1}{\phi}\left(\frac{\langle \sigma^f_{11} - \sigma^{f0}_{11} \rangle - \langle \sigma^f_{22} - \sigma^{f0}_{22} \rangle}{Wi}\right), \tag{33}$$

and the stresslet contribution as

$$\frac{S_{11-22}}{Wi} = \frac{1}{\phi}\left(\frac{-\langle x_1 f_1 \rangle + \langle x_2 f_2 \rangle}{Wi}\right). \tag{34}$$

D. Validation

In this section, we present a validation of our BF and IB simulations in transient shear. To validate BF simulations, we compare the PIFS and stresslet values from numerical simulations at a small $Re = 0.05$ with the semianalytical expressions from a new theory that we develop for the time-dependent evolution of average stress in a dilute suspension valid for $\mathrm{Wi} \ll 1$. The shear flow begins at time $t = 0$. We show the complete derivation of the semianalytical expressions of PIFS and stresslet contributions through $\mathrm{O}(\mathrm{Wi}^2)$ at $Re = 0$ in an Oldroyd-B fluid in the Appendix. We present the final expressions below. The average stress in a suspension can be written as a perturbation series in Wi,

$$\langle \sigma_{ij} \rangle = \langle \sigma^{(0)}_{ij} \rangle + Wi\langle \sigma^{(1)}_{ij} \rangle + Wi^2 \langle \sigma^{(2)}_{ij} \rangle + \ldots. \tag{35}$$

The complete expression for the time-dependent evolution of

$\langle\sigma_{ij}^{(0)}\rangle$ is

$$\begin{aligned}\langle\sigma_{ij}^{(0)}\rangle &= \text{Isotropic Terms} + 2\beta E_{ij}H(\tau)\\ &\quad + 2(1-\beta)E_{ij}(1-exp(-\tau))\\ &\quad + 5\phi\beta E_{ij}H(\tau) + 5\phi(1-\beta)E_{ij}(1-\exp(-\tau)).\end{aligned} \tag{36}$$

For higher order stress terms $\langle\sigma_{ij}^{(1)}\rangle$ and $\langle\sigma_{ij}^{(2)}\rangle$, we find the time-dependent functional form only and do not compute the constant coefficients of these time-dependent functions analytically. The expressions are

$$\langle\sigma_{ij}^{(1)}\rangle = (1-\beta)\phi A_{ij}(1-\exp(-\tau)-\tau\exp(-\tau)), \tag{37}$$

$$\begin{aligned}\langle\sigma_{ij}^{(2)}\rangle &= B_{ij}\phi\left[1-\exp(-\tau)-\tau\exp(-\tau)-\frac{\tau^2}{2}\exp(-\tau)\right]\\ &\quad + C_{ij}\phi\left[\beta(1-\exp(-\tau)-\tau\exp(-\tau))\right.\\ &\quad \left.-\frac{\beta}{2(1-\beta)}\tau^2\exp(-\tau)+\frac{\beta^3}{(1-\beta)^2}\tau\exp(-\tau)\right]\\ &\quad + C_{ij}\phi\left[-\frac{\beta^4}{(1-\beta)^3}(\exp(-\tau)-\exp(-\tau/\beta))\right]\\ &\quad + D_{ij}\phi\left[\beta(1-\exp(-\tau)-\tau\exp(-\tau))\right.\\ &\quad \left.-\frac{\beta^3}{(1-\beta)^2}(\exp(-\tau/\beta)-\exp(-\tau))\right]\\ &\quad + D_{ij}\phi\left[-\frac{\beta^3}{(1-\beta)}\left(\exp(-\tau)-\exp\left(-\frac{1+\beta}{\beta}\tau\right)\right)\right]\\ &\quad + D_{ij}\phi\left[-\frac{\beta}{(1-\beta)}(\tau\exp(-\tau)-\exp(-\tau)+\exp(-2\tau))\right],\end{aligned} \tag{38}$$

where $\tau = \frac{t}{\lambda}$, E_{ij} is the rate of strain tensor, and β is the ratio of solvent viscosity to the total zero shear viscosity defined previously. For shear flow, there is no O(Wi) correction to the transient shear stress of dilute suspensions; therefore, $A_{ij} = 0$. We find the values of the coefficients B_{12}, C_{12}, and D_{12} in the above Eq. (38) by fitting to the transient shear numerical simulations data at three small Wi = 0.1, 0.2, and 0.3 simultaneously. There is no O(1) or O(Wi) correction to the PIFS and the first correction comes at O(Wi^2). Thus, the analytical expression for the PIFS has the same functional form as $\langle\sigma_{ij}^{(2)}\rangle$, and we find the coefficients by fitting to the time-dependent numerical PIFS values using nonlinear least squares regression. The stresslet has a Newtonian contribution at O(1), and we also need to determine the coefficients at O(Wi^2). We follow the same procedure to find the coefficients for the stresslet expression by fitting to numerical data. We show the BF simulation results and the best theoretical fits for the PIFS in Fig. 4(a) and stresslet in Fig. 4(b). The values of the fit parameters are $B_{12} = 2.486$, $C_{12} = -0.537$, and $D_{12} = -2.152$ for the PIFS, and the steady state value of the PIFS is then given by $B_{12} + C_{12}\beta + D_{12}\beta = 0.658$ that agrees with steady state theory of the PIFS derived by Einarsson *et al.* [20] as shown in Fig. 5(a). We find the values of the fit parameters $B_{12} = -0.029$, $C_{12} = 0.122$, and $D_{12} = -0.628$ for the stresslet and Newtonian stresslet comes out to be $S_{12}^{Newt} = 2.457$. We then compare the steady state value of stresslet from above equation $B_{12} + C_{12}\beta + D_{12}\beta = -0.373$ with the steady state theory for the particle stresslet derived by Einarsson *et al.* [20] in Fig. 5(b) and find that the two values are again quite close. The above comparisons show that the time-dependent behavior in numerical simulations is in good agreement with theoretical predictions for the transient response of dilute suspensions in the limit of small Wi values. There is discrepancy in the PIFS agreement at small strains for small Wi values, which arises due to the difference in the nature of flow at time $t = 0$ between numerical simulations and theory. The numerical simulations start from the steady state Newtonian flow field, whereas the theory assumes the start-up from rest at time $t = 0$.

To validate IB simulations, first we show the comparison of steady values of relative viscosity η_r of Newtonian suspensions at finite particle concentration obtained from our IB simulations against theoretical relations—Kreiger–Dougherty relation [21] $\eta_r = (1-\frac{\phi}{\phi_{\max}})^{-2.5\phi_{\max}}$ and $O(\phi^2)$ theory of Batchelor and Green [22] $\eta_r = 1 + 2.5\phi + 7.6\phi^2$ in Fig. 6. There is excellent quantitative agreement between IB

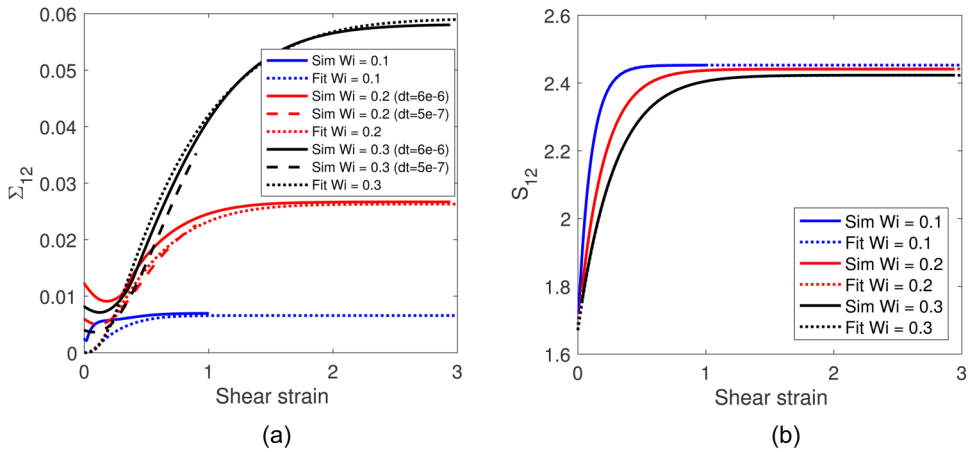

FIG. 4. Comparison of PIFS (a) and stresslet (b) contributions with small Wi theory as a function of shear strain for a range of Wi simulated using the Oldroyd-B model. The parameters of Oldroyd-B model used in transient shear simulations are $\beta = 0.68$.

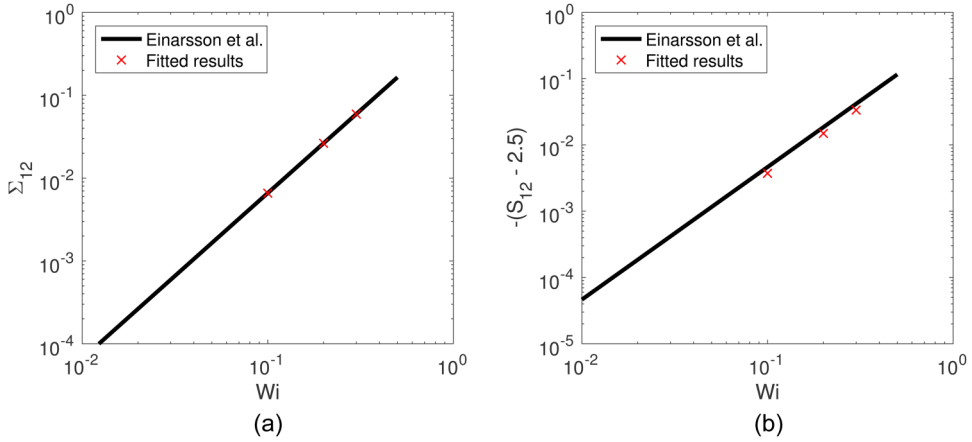

FIG. 5. Comparison of steady state PIFS (a) and stresslet (b) contributions calculated using fitted parameters B_{12}, C_{12}, and D_{12} with the theory of Einarsson *et al.* for a range of small Wi simulated using the Oldroyd-B model. The parameters of the Oldroyd-B model used in transient shear simulations are $\beta = 0.68$.

simulation results and theoretical relations. Next, we compare the time-dependent evolution of stresses from IB simulations for a single sphere with BF simulations at Wi = 3 in transient shear flow. We show the comparison of the PIFS and stresslet as a function of shear strain between BF and IB simulations in Fig. 7(a) and comparison of the per-particle viscosity as a function of shear strain between BF and IB simulations in Fig. 7(b). There is excellent agreement between the IB and BF simulations, which gives us confidence that our method for the calculation of the PIFS and stresslet in IB simulations is reliable and the IB simulations can be used for calculating the bulk stress in nondilute suspensions.

III. NUMERICAL RESULTS

A. BF simulations for dilute particle suspensions in Dai's Boger fluid

We perform BF simulations for dilute particle suspensions (i.e., single particles) in a computational domain of size $40a \times 40a \times 40a$ at $Re = 0.05$ with the suspending polymeric fluid modeled using both the Oldroyd-B equation and the Giesekus equation. The parameters of both models are chosen such that they fit to the steady shear rheology of the Boger fluid used by Dai *et al.* [4] ($\beta = 0.68$, $\alpha = 0$ for the Oldroyd-B and $\beta = 0.68$, $\alpha = 0.0039$ for the Giesekus model). We use this fluid simply as an example of a Boger fluid to provide model calculations. We show the evolution of the PIFS and stresslet with shear strain for small Wi = 0.1, 0.2, and 0.3 using the Oldroyd-B model in Fig. 5, and the PIFS and stresslet for finite values of Wi = 0.3, 0.5, 0.8, 1, 2, 3, and 4 using the Giesekus model in Fig. 9. The per-particle viscosity for finite Wi values are shown in Fig. 8. The simulations are mesh-converged and time-converged as the results change by less than 8% when we decrease the mesh size by a factor of 2 and the time step by a factor of 4. The angular velocity of the sphere is updated at each time step such that the nondimensional torque on the sphere is less than 1×10^{-3} at all times.

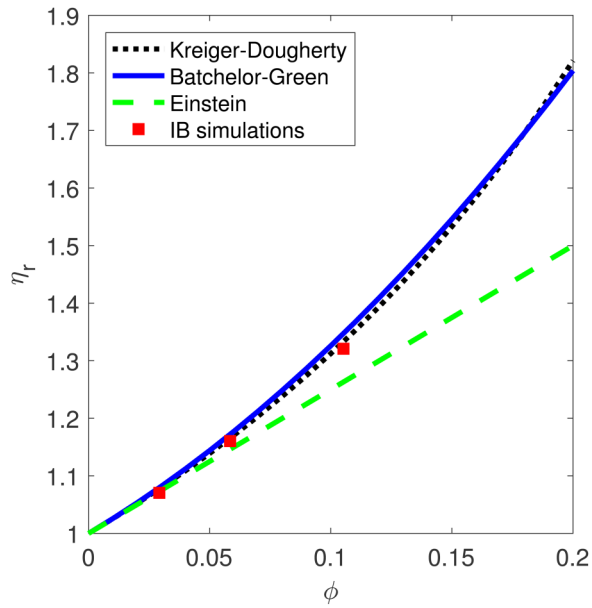

FIG. 6. Comparison of relative viscosity η_r of Newtonian suspensions between the IB simulations, the Kreiger–Dougherty relation, the Batchelor–Green theory, and the Einstein relation.

We observe in Fig. 8 that the per-particle viscosity increases monotonically to steady state for different Wi and the steady state per-particle viscosity increases with Wi consistent with steady shear simulations [13]. This means the particles cause the viscosity of the suspension to shear-thicken although their presence does not change the qualitative evolution of the shear stress in the suspension compared to the behavior of the suspending fluid. Note that the per-particle viscosity requires increased strain to reach steady state at higher values of Wi in Fig. 8. The evolution of the PIFS and stresslet in Fig. 9 shows that the PIFS increases monotonically to steady state, but the stresslet shows an overshoot to steady state at higher Wi values. The values of the steady state PIFS increase with Wi but the steady state stresslet values decrease with Wi, again consistent with simulations found elsewhere [13]. The increase in PIFS offsets the decrease in the stresslet leading to a net shear thickening of the suspension. The decrease in stresslet values with Wi can be understood as the polymer stretch surrounding a given particle "shields" the particle and thus reduces the local surface tractions. We believe the same "shielding" effect leads to nonmonotonicity in the stresslet evolution with strain

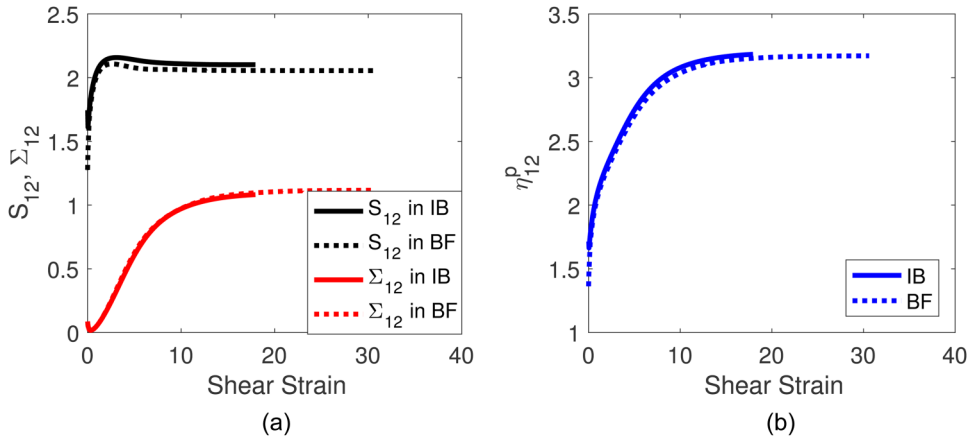

FIG. 7. Comparison of PIFS Σ_{12} and stresslet S_{12} (a) and per-particle viscosity η^p_{12} (b) between BF and IB simulations at Wi = 3. The BF simulations were performed for a single sphere suspended in a box of size 40a × 40a × 40a whereas IB simulations were performed for a single sphere suspended in a box of size 15a × 20a × 7.5a.

at high Wi numbers. The stresslet values start to increase at small strains as the suspension behaves like a Newtonian suspension. However, increasing polymer stretch in the fluid with strain shields the particle surface and reduces local surface tractions, leading to nonmonotonicity at finite strains.

We also show the per-particle contribution to the first normal stress difference coefficient $\psi_1^p = \Sigma_{11-22}/\mathrm{Wi} + S_{11-22}/\mathrm{Wi}$ with shear strain for different Wi values in Fig. 10 and the evolution of $\Sigma_{11-22}/\mathrm{Wi}$ and S_{11-22}/Wi contributions in Fig. 11. All three quantities ψ_1^p, $\Sigma_{11-22}/\mathrm{Wi}$, S_{11-22}/Wi increase monotonically to steady state, but the steady state values of ψ_1^p and $\Sigma_{11-22}/\mathrm{Wi}$ are nonmonotonic with Wi as witnessed elsewhere [13]. Up to Wi = 2, the particles cause the first normal stress difference coefficient of the suspension to shear-thicken relative to the suspending fluid. Again, this can be attributed to the increase in the PIFS contribution with increasing Wi. Beyond Wi = 2, however, the PIFS contribution starts decreasing with Wi and, combined with the decreasing stresslet contribution, the overall behavior becomes shear-thinning. The steady state values of ψ_1^p, $\Sigma_{11-22}/\mathrm{Wi}$, and S_{11-22}/Wi are consistent with other simulation results [13].

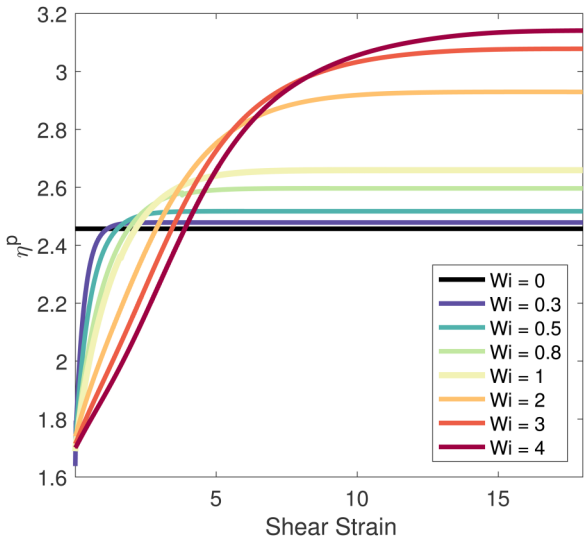

FIG. 8. Evolution of per-particle viscosity contribution to shear stress η^p_{12} with shear strain for a range of Wi simulated using the Giesekus model. The parameters of the Giesekus model used in transient shear simulations are $\beta = 0.68$ and $\alpha = 0.0039$. These parameters model the shear rheology of Dai's Boger fluid [4].

B. BF and IB simulations for particle suspensions in the B25 Boger fluid

As presented above, we have performed IB simulations for a single sphere in a box of size $L_1 = 15a \times L_2 = 20a \times L_3 = 7.5a$ in dilute limit with characteristic mesh size $h = a/10$ to compare with BF simulations in Fig. 7, and we achieved excellent agreement. We know from previous studies that this domain size is sufficiently large to reproduce "unbound" dilute suspension results [13]. We next present IB simulation results in the nondilute limit for three different particle volume fractions $\phi = 2.5\%$, 5%, and 10% with the same size computation box of dimensions $L_1 = L_3 = 7.5a$ and $L_2 = 15a$ and change the number of particles in the box to vary the volume fraction ($N = 5$ for $\phi = 2.5\%$, $N = 10$ for $\phi = 5\%$, and $N = 18$ for $\phi = 10\%$). The domain dimension in the flow gradient direction was chosen to be larger in order to minimize wall effects. The initial configurations are randomly generated with the following excluded-volume constraints: (1) The center of mass of each particle is at least $2.5a_{eff}$ from the center of mass of another particle and (2) the center of mass of each particle is at least a $2a_{eff}$ from the walls at $y = \pm L_2/2$. We define the effective particle radius to be the sum of nominal particle radius, "a" and the Eulerian mesh size, "h" as $a_{eff} = a + h/2$, thus accounting for the transition region of the interface. The simulations are performed for a total strain of $\dot{\gamma}t \geq 30$ and the transient stress calculated in simulations is recorded. We run three simulations for a given ϕ with different initial distribution of spheres and average over those simulations to obtain somewhat smoother average results.

For the multiparticle simulations, we apply a short-range interparticle force, taken from the study [23], to prevent simulated particles from overlapping each other or the wall.

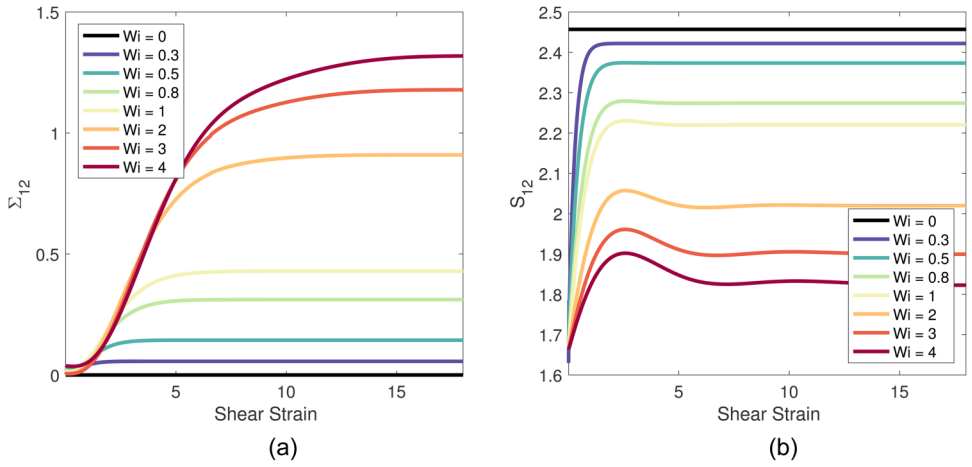

FIG. 9. Evolution of PIFS (a) and stresslet (b) contributions to per-particle viscosity η^p_{12} with shear strain for a range of Wi simulated using the Giesekus model. The parameters of the Giesekus model used in transient shear simulations are $\beta = 0.68$ and $\alpha = 0.0039$.

The form of that force is as follows:

$$F_i[a, b] = A\left[MAX\left(0, \frac{h-d}{h}\right)\right]^2 \frac{x_i[a] - x_i[b]}{\|x_i[a] - x_i[b]\|}, \qquad (39)$$

where a and b denote two rigid surfaces, d is the separation distance between those surfaces, h is the characteristic mesh size and also the range of the collision force, and A is a prefactor. We use the calculated stress on the wall to compute bulk shear stress as shown in Eq. (21), and we see less than 5% error between these calculations and those obtained from rhs in Eq. (21). This can be seen in the calculation of per-particle viscosity using Eqs. (24a) and (24b) as shown in Fig. 12 for different particle volume fractions.

We perform BF and IB simulations for dilute and nondilute particle suspensions in a polymeric fluid, modeled by four-mode Oldroyd-B parameters shown in Table I. The parameters are obtained from the linear viscoelastic data of the B25 Boger fluid shown in Sec. IV below as we will compare our simulation results with experiments for this suspending fluid in Sec. V. The time evolution of per-particle viscosity η^p_{12} as a function of shear strain in the dilute limit and for varying ϕ values at Wi= 3 and Wi = 6 is shown in Fig. 12. The solid lines show the calculation according to Eq. (24a), and the dotted lines show the calculation according to Eq. (24b). We get excellent agreement between the two approaches as expected although the calculation from Eq. (24b) shows more fluctuations because the IB force on particles changes rapidly to prevent them from colliding with other particles. Therefore, we use Eq. (22a) for the calculation of the stresslet and Eq. (24a) for the calculation of per-particle viscosity in the rest of the paper. We note three key points from the simulation results—the per-particle viscosity (1) from single-particle BF simulations matches with multiple-particle IB simulation for 2.5% suspension, which implies 2.5% suspension is in dilute limit since particle-particle hydrodynamic interactions do not make any difference, (2) evolves monotonically to steady state with shear strain in BF and IB simulations for all ϕ values, and (3) steady values increase with ϕ in IB simulations.

We also present the evolution of the per-particle contribution to the first normal stress difference coefficient ψ^p_1 using BF simulations in the dilute limit and IB simulations for varying ϕ [according to Eq. (32)] at Wi = 3 and Wi = 6 in Fig. 13. We note that ψ^p_1 in IB simulations is independent of ϕ at both Wi = 3 and Wi = 6 for all shear strains, and the values are somewhat smaller compared to BF simulations. This suggests that a finer Eulerian mesh is needed in IB simulations to match with BF simulations in the first normal stress difference and that these are a weak function of volume fraction.

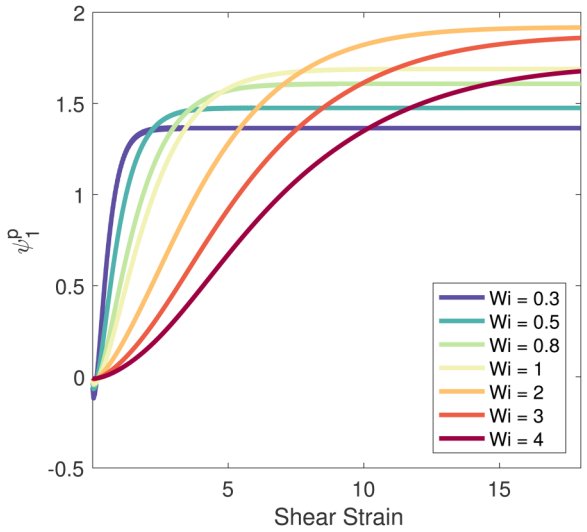

FIG. 10. Evolution of per-particle contribution to first normal stress difference coefficient ψ^p_1 with shear strain for a range of Wi simulated using the Giesekus model. The parameters of the Giesekus model used in transient shear simulations are $\beta = 0.68$ and $\alpha = 0.0039$.

IV. EXPERIMENTS

We now present experimental measurements of the rheology of different suspensions in the B25 Boger fluid.

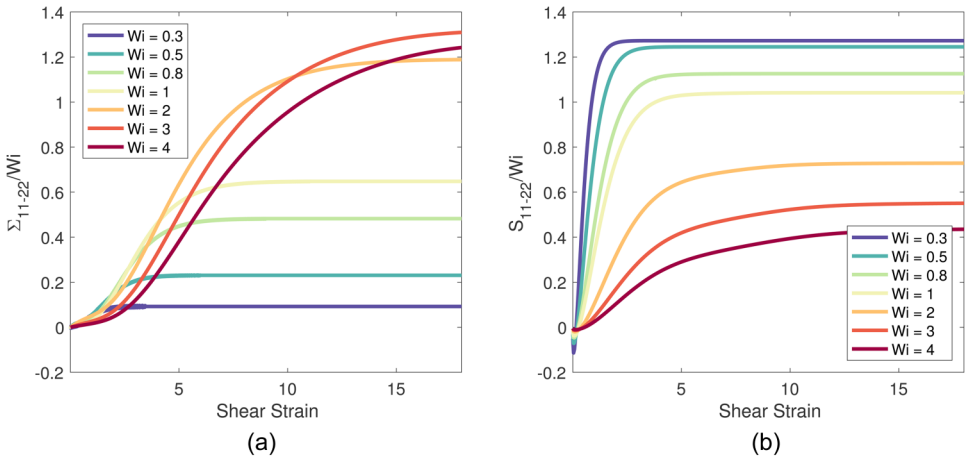

FIG. 11. Evolution of PIFS (a) and stresslet (b) contributions to first normal stress difference coefficient ψ_1^p with shear strain for a range of Wi simulated using Giesekus model. The parameters of Giesekus model used in transient shear simulations are $\beta = 0.68$ and $\alpha = 0.0039$.

A. Materials

The B25 Boger fluid we use in our experiments consists of a high molecular weight polyisobutylene [(PIB) average $M_w \approx 4.2 \times 10^6$ from Sigma-Aldrich] dissolved in kerosene and mixed with low molecular weight polybutene [(PB) Indopol H-25 from Ineos Oligomers Technology]. We made the solution of PIB in kerosene first by dissolving small pieces of PIB (3.4 wt. %) in kerosene (96.6 wt. %) and then added PB for a final fluid composition of 92.93 wt. % of PB, 6.83 wt. % of kerosene, and 0.24 wt. % of PIB. We found the density of the fluid to be $810\,\mathrm{kg/m^3}$. This B25 Boger fluid is similar to the benchmark Boger M1 fluid [24], although the PIB we used has a higher M_w (4.2×10^6 versus 3.8×10^6) [25].

The dispersed phase consists of polyethylene microspheres purchased from Cospheric. The particle diameter ranges from 32 to 38 μm, screened such that 90% are in the specified size range. The density of the particles is reported to be $960\,\mathrm{kg/m^3}$. The small density mismatch between the particles and the B25 fluid does not lead to significant sedimentation effects given the time scale of the experiments. Particles settle at most 1 diameter during the course of an experiment, based on the Stokes drag of the particles. Inertial effects are also insignificant; the Reynolds number based on the shear rate and the particle radius is less than 6×10^{-7}. The particles are also large enough such that Brownian stresses can be ignored (Peclet number $>7 \times 10^7$).

B. Rheology of the suspending fluid

We characterized the steady and dynamic shear properties of the suspending fluid and the suspensions with an ARES-G2 rheometer using the 25 mm diameter cone-and-plate geometry. All the measurements in the study were made at temperature $T = 19.5\,^{\circ}\mathrm{C}$. We show the small amplitude oscillatory shear data of the B25 fluid at two strain amplitudes $\gamma = 10\%$ and 40% in Fig. 14(a). The data for the two strain amplitudes are identical, which suggests that we are in the linear response regime of the fluid. We also performed the strain amplitude sweep at an angular frequency of 1 rad/s and found the

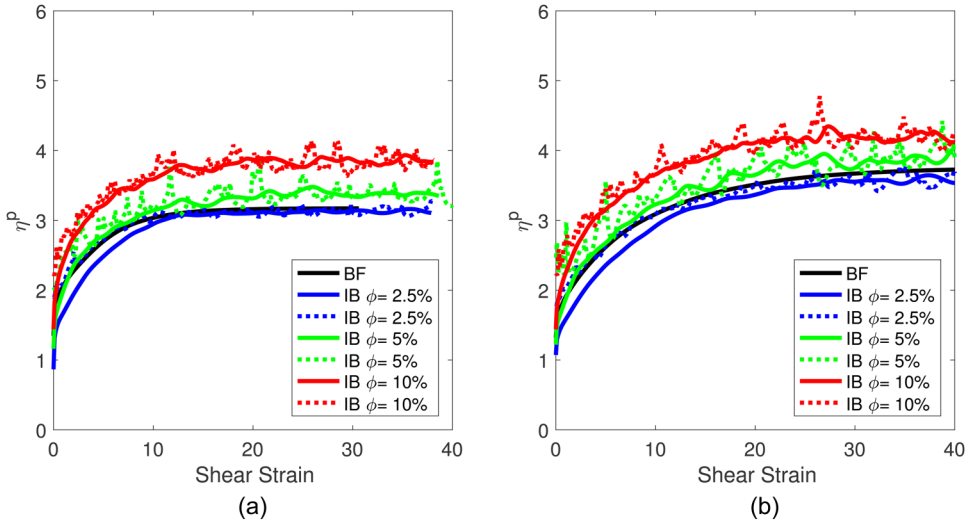

FIG. 12. Evolution of per-particle viscosity η_{12}^p as a function of shear strain for different particle volume fractions $\phi = 2.5\%$, 5%, and 10% at largest Wi = 3 (a) and Wi = 6 (b) in IB simulations. The solid lines show the calculation according to Eq. (24a), and the dotted lines show the calculation according to Eq. (24b). Also shown in the black solid line is the BF simulation result for dilute suspension at the same Wi values.

TABLE I. MM Oldroyd-B parameters for the B25 fluid found by fitting to linear viscoelastic data and stress relaxation data simultaneously in Fig. 14.

Mode	Viscosity (Pa s)	Relaxation time (s)
1	0.6699	1.0025
2	0.3459	0.1697
3	0.2165	0.0537
4	0.2745	0.0038
Solvent	1.6103	…

response of fluid to be independent of strain amplitude until $\gamma = 100\%$. We show the stress relaxation data when a step strain amplitude of $\gamma = 500\%$ is applied to the B25 fluid in Fig. 14(b). We performed stress relaxation experiments at this value of strain amplitude to reduce the noise in the data found at lower values of strain amplitude.

To fit these data, we obtain the best four-mode and one-mode Oldroyd-B parameters $(\eta_{p,k}, \lambda_k)$ by fitting to the SAOS and the stress relaxation data simultaneously using nonlinear least squares regression. The parameters are shown in Tables I and II. We used the Levenberg–Marquardt regression method to minimize the error between the experimentally measured values and the values determined from linear viscoelastic theory at the same angular frequencies. We show the four-mode and one-mode model predictions for the dynamic viscosity η' and storage modulus G' in Fig. 14(a). We see that the four-mode model predictions agree very well with the experimental data, but the one-mode model is not able to capture the increase in storage modulus G' values at high angular frequencies. Both the single-mode (SM) and multimode (MM) models capture the stress relaxation data reasonably well in Fig. 14(b), and the longest relaxation time in both models is close.

Next, we show the steady shear measurements of the B25 fluid, viscosity η, first normal stress difference N_1, and first normal stress coefficient ψ_1 as a function of shear rate in Fig. 15. The B25 fluid behaves as a Boger fluid with nearly constant viscosity and the primary normal stress coefficient. Thus, the Oldroyd-B model is an appropriate closed-form constitutive model for characterizing the shear properties of the fluid in the range of shear rates shown. The four-mode Oldroyd-B model parameters that we obtained from the linear viscoelastic data of the B25 fluid overpredict the steady values of the first normal stress difference N_1 and coefficient ψ_1 in Fig. 15. So, we find another set of MM Oldroyd-B parameters by fitting to the steady shear data alone and report $\eta_{p,k}, \lambda_k$ from this fit in Table III. We note that the longest relaxation time for these parameters is 0.73 s and thus smaller when compared to the 1 s that we obtained from the linear data. The difference in fitted parameters can be expected given that the steady shear measurements probe the nonlinear response of the polymeric fluid at high shear rates, whereas SAOS measurements capture the linear response of the fluid.

Next, we present the transient shear measurements in the start-up of shear for the B25 fluid as a function of shear strain for three different applied shear rates in Fig. 16. The viscosity of the suspending B25 fluid increases monotonically to steady state for all the shear rates investigated. We also plot the predictions of the two MM Oldroyd-B models that we obtained from fitting to the (1) linear viscoelastic data and (2) steady shear data, in the same figure. The MM model from the linear viscoelastic data provides a reasonable prediction of the time evolution of stress in the B25 fluid at a small shear rate of $\dot{\gamma} = 1\,\mathrm{s}^{-1}$ or $\mathrm{Wi} = 1$, but the agreement between this model and experimental data worsens at the highest shear rate studied $\dot{\gamma} = 6\,\mathrm{s}^{-1}$ or $\mathrm{Wi} = 6$. The MM model based on the linear data takes longer to reach steady state compared to the experimental data at higher values of Wi. The time evolution of the experimental data at the highest shear rate $\dot{\gamma} = 6\,\mathrm{s}^{-1}$ is captured very well by the other MM model obtained from the steady shear data alone in Table III. This makes some sense because the response of the fluid becomes nonlinear at high shear rates such as $\dot{\gamma} = 6\,\mathrm{s}^{-1}$, and one might expect the MM model from the fit

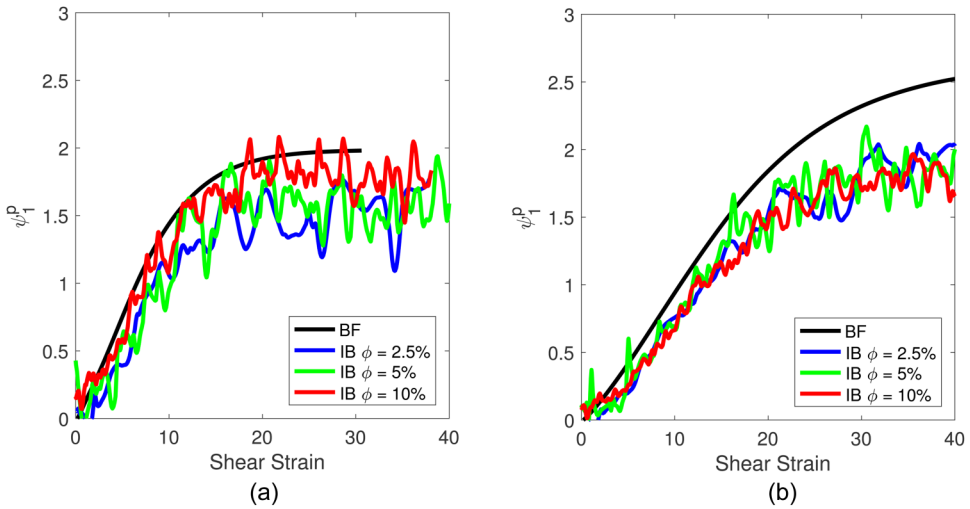

FIG. 13. Evolution of per-particle first normal stress difference coefficient ψ_1^p as a function of shear strain for different particle volume fractions $\phi = 2.5\%$, 5%, and 10% at largest $\mathrm{Wi} = 3$ (a) and $\mathrm{Wi} = 6$ (b) in IB simulations. Also shown in the black solid line is the BF simulation result for dilute suspension at the same Wi values.

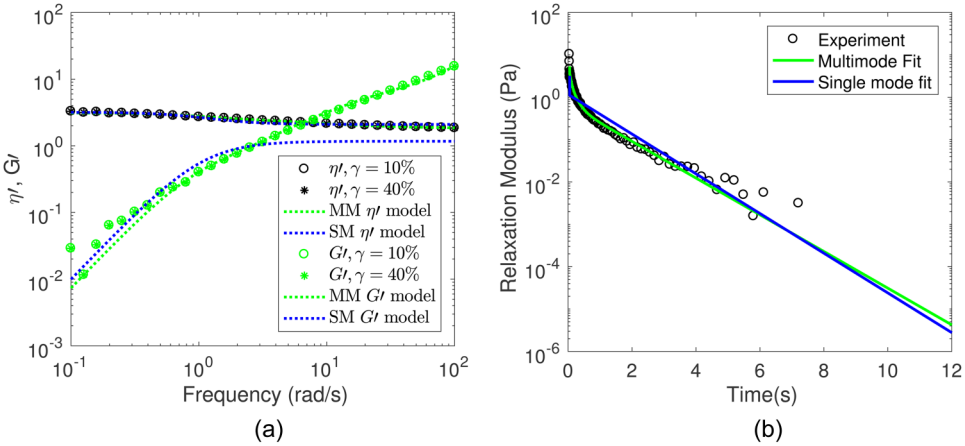

FIG. 14. Experimental frequency sweep (a) and stress relaxation (b) data of the B25 fluid. Also shown are the MM and SM model predictions for both the frequency sweep and stress relaxation data. The MM fit parameters are shown in Table I and SM parameters are shown in Table II.

to the steady nonlinear data of the B25 fluid to do a better job at predicting the time-dependent response.

C. Rheology of suspensions

We show the SAOS data of different particle volume fraction suspensions in the B25 fluid at two strain amplitudes $\gamma = 10\%$ and 40% in Fig. 17. The data for the two strain amplitudes are very close, which suggests that we are in the linear response regime of the different particle volume fraction suspensions. The dynamic viscosity η' and the storage modulus G' of the suspensions increase with ϕ at all angular frequencies. To compare to these measurements, we derive a theory for analytical calculation of η' and G' at different particle volume fraction suspensions in an Oldroyd-B fluid and show the details of the derivation in the Appendix. A similar expression has been suggested elsewhere in the literature [1]. The equations for G' and η' when the suspending fluid is modeled by a four-mode Oldroyd-B model become

$$G' = \sum_{k=1}^{k=4} \frac{\eta_{p,k}\lambda_k\omega^2}{1+(\lambda_k\omega)^2}[1+f(\phi)], \tag{40}$$

$$\eta' = \eta_s[1+f(\phi)] + \sum_{k=1}^{k=4} \frac{\eta_{p,k}}{1+(\lambda_k\omega)^2}[1+f(\phi)]. \tag{41}$$

The function $f(\phi)$ is the extra viscosity function for a Newtonian suspension that includes all hydrodynamic interactions between particles at zero Reynolds number. For example, $f(\phi) = 2.5\phi$ for dilute suspensions $\phi \ll 1$. The function $1+f(\phi)$ is a measure of the relative viscosity η_r of Newtonian suspensions. The solid lines in Fig. 17 correspond to linear viscoelastic (LVE) theoretical Eqs. (40) and (41) with η_r taken from the $O(\phi^2)$ theory of Batchelor and Green [22] for Newtonian nondilute suspensions, $\eta_r = 1 + 2.5\phi + 7.6\phi^2$. We also plot the LVE theoretical predictions for another semiempirical η_r relation by Kreiger and Dougherty [21] $\eta_r = (1-\frac{\phi}{\phi_{\max}})^{-2.5\phi_{\max}}$ in the same Fig. 17. The Kreiger–Dougherty relation is a semiempirical correlation for effective viscosity of solid-liquid suspensions, which is valid for a full range of particle volume fractions. This relation reduces to the linear form $\eta_r = 1 + 2.5\phi$ at very low particle concentrations, and at some characteristic particle volume fraction $\phi_{\max}$, the relative viscosity becomes infinite. The quantity $\phi_{\max}$ is called the packing fraction since the approach to infinite viscosity is usually ascribed to the attainment of a close-packed structure. The theory with two different η_r definitions predict the measured dynamic viscosity very well at small angular frequencies but shows

TABLE II. SM Oldroyd-B parameters for the B25 fluid found by fitting to linear viscoelastic data and stress relaxation data simultaneously in Fig. 14.

Mode	Viscosity (Pa s)	Relaxation time (s)
1	1.085	0.926
Solvent	2.0932	…

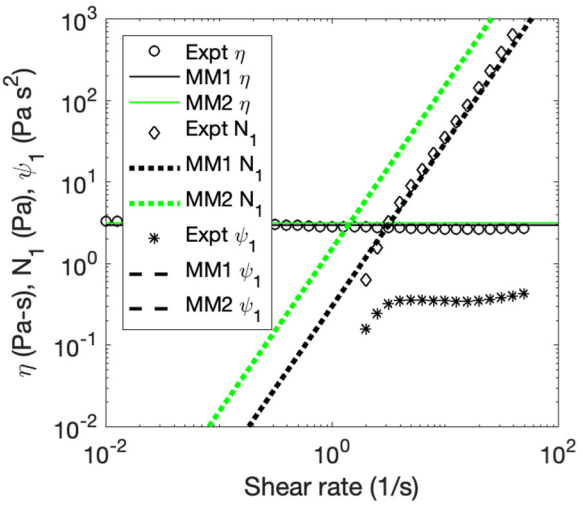

FIG. 15. Steady shear data of the B25 fluid and predictions of the MM model from linear data (called MM2 in the plot). This model overpredicts the first normal stress difference N_1 and the first normal stress coefficient ψ_1. So we fit another MM model to steady shear data alone (called MM1 in the plot) and show the parameters in Table III.

TABLE III. MM Oldroyd-B parameters for the B25 fluid found by fitting to steady shear data alone in Fig. 15.

Mode	Viscosity (Pa s)	Relaxation time (s)
1	0.1695	0.7380
2	0.1519	0.1271
3	0.1156	0.0204
4	0.0783	0.0009
Solvent	2.4098	…

somewhat stronger shear-thinning behavior than found in experiments at higher frequencies. Nonetheless, the agreement is still quite good. The theory predicts experimental values of the storage modulus G' fairly accurately for all particle volume fraction suspensions. Note the theoretical predictions of the dynamic viscosity and the storage modulus using the two η_r definitions are within the error of the measurements.

We also show experimental measurements of the steady state viscosity η_{ss}, the steady state first normal stress difference N_1 and the primary normal stress coefficient ψ_1 as a function of shear rate for different particle volume fractions in Fig. 18. The viscosity shows a plateau at small shear rates in the limit $\mathrm{Wi} \to 0$ for all ϕ. The suspensions with $\phi = 2.5\%$, 5%, 10%, and 20% show shear-thickening behavior at high shear rates as opposed to the slight shear-thinning behavior of the suspending B25 fluid. These observations are in agreement with the measurements reported in the literature [4,5]. The first normal stress coefficient of all suspensions increases with the shear rate modestly, and the values for the 20% suspension are significantly higher than other particle volume fractions at all shear rates. The difference in ψ_1 values becomes appreciable at shear rates of $10\,\mathrm{s}^{-1}$ or higher for lower particle volume fraction suspensions (i.e., $< 20\%$).

Next, we present the time-dependent evolution of shear stress for the same particle volume fraction suspensions $\phi = 2.5\%$, 5%, 10%, and 20% in the suspending B25 fluid at shear rates $\dot{\gamma} = 1$, 3, 6, and s^{-1} in Fig. 19. The evolution is monotonic to steady state for all particle suspensions just like the evolution in a suspending Boger fluid although the time to reach steady state increases with the particle volume fraction at a given shear rate. As an example, let us look at the experimental data at a shear rate of $3\,\mathrm{s}^{-1}$ where the 20% suspension does not reach steady state in 40 strain units but the 2.5% suspension reaches steady state in about 20 strain units. The time to reach steady state also increases with the shear rate for a given particle volume fraction in the suspension. These measurements reinforce the idea that it is important to study the transient shear rheology of suspensions in viscoelastic fluids where it may take anywhere from 20 to 300 strain units to reach steady state.

We also show the evolution of the first normal stress difference coefficient ψ_1 as a function of shear strain for suspensions in Fig. 20. There is significant noise in the data at a shear rate of $1\,\mathrm{s}^{-1}$ for all suspensions investigated, but the signal becomes clearer at higher shear rates. Therefore, we show measurements for higher shear rates $\dot{\gamma} = 3$ and $6\,\mathrm{s}^{-1}$. The first normal stress difference coefficient ψ_1 values are very close for $\phi = 0\%$, 2.5%, 5%, and 10% for shear rates $\dot{\gamma} \leq 3\,\mathrm{s}^{-1}$, but the value for 20% suspension is higher compared to that of the suspending fluid. At the highest shear rate investigated, $\dot{\gamma} = 6\,\mathrm{s}^{-1}$, the difference between ψ_1 values for $\phi = 20\%$, 10%, and 0% is clear, but 2.5% and 5% suspensions have values very close to that of the suspending fluid.

We calculate the per-particle contribution to viscosity and first normal stress difference coefficient of suspensions from experimental data for different ϕ values and shear rates to compare with the BF and IB simulations in Sec. V. We compute the per-particle contribution to the suspension viscosity and the suspension first normal stress coefficient by subtracting the fluid contribution from the relevant suspension quantity and dividing the difference by the particle volume fraction ϕ, as shown below,

$$\eta^p = \frac{\eta^\phi - \eta^{\phi=0}}{\phi}, \tag{42}$$

and

$$\psi_1^p = \frac{\psi_1^\phi - \psi_1^{\phi=0}}{\phi}. \tag{43}$$

The first normal stress difference coefficient is

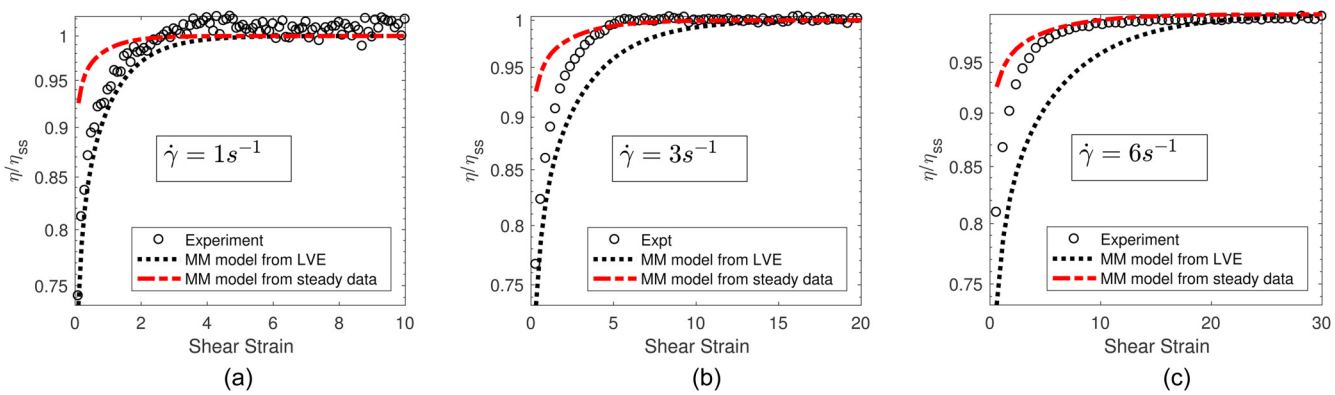

FIG. 16. Transient shear data of the B25 fluid from experiments at shear rates of 1 (a), 3 (b), and $6\,\mathrm{s}^{-1}$ (c). Also shown are the predictions of the MM model from frequency sweep and stress relaxation data in dots and the MM model from steady shear data alone in dashes.

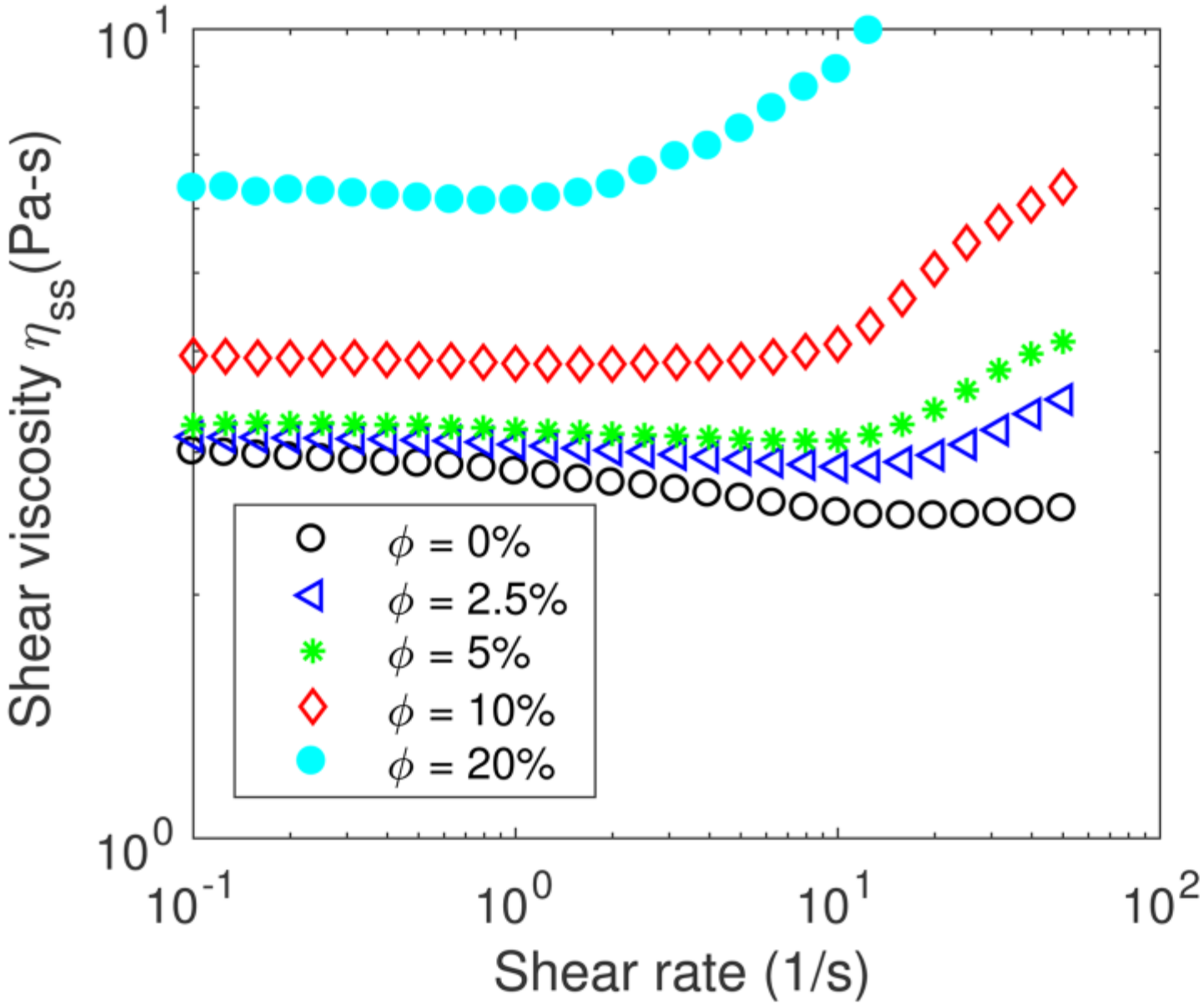
Shear viscosity η_{ss} (Pa-s)
10^1
10^0
10^{-1}
10^0
10^1
10^2
Shear rate (1/s)
ϕ = 0%
ϕ = 2.5%
ϕ = 5%
ϕ = 10%
ϕ = 20%

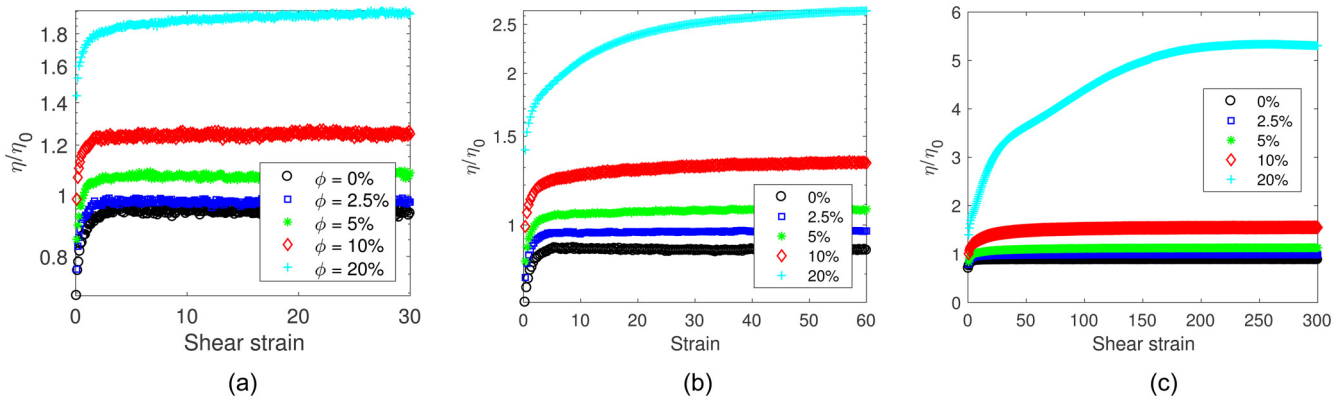

FIG. 19. Experimental measurements of the B25 fluid and four other particle volume fraction suspensions with ϕ ranging from 2.5% to 20% in transient shear flow at shear rates of 1 (a), 3 (b), and 6 s^{-1} (c).

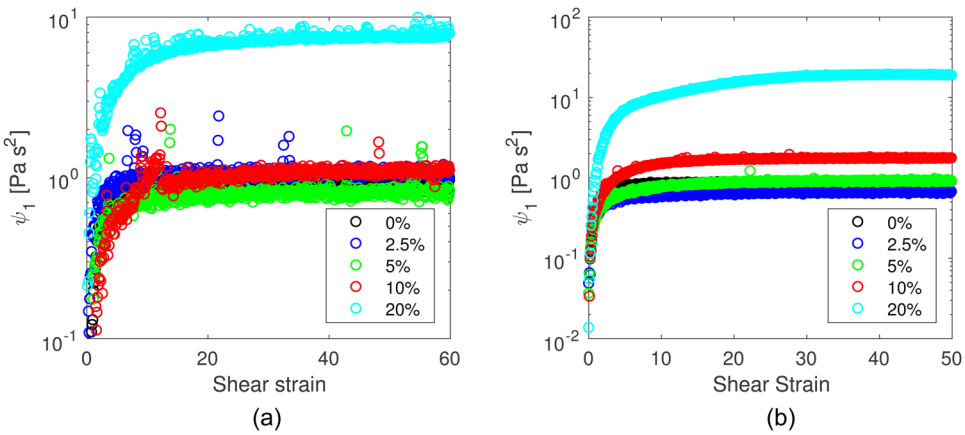

FIG. 20. Experimental measurements of first normal stress difference coefficient of the B25 fluid and four other particle volume fraction suspensions with ϕ ranging from 2.5% to 20% in transient shear flow at shear rates of 3 (a) and 6 s^{-1} (b).

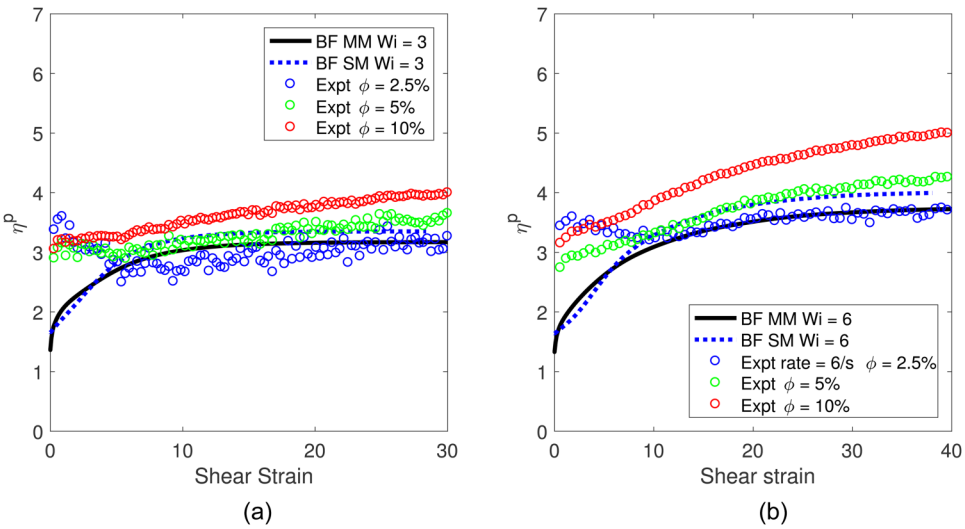

FIG. 21. Comparison of per-particle viscosity η^p from experimental data at shear rates of 3 (a) and 6 s^{-1} (b) for $\phi = 2.5\%$, 5%, and 10% suspensions in the B25 Boger fluid with single-particle BF simulations at the same largest Wi. The simulation results are shown for the MM Oldroyd-B model in the solid line and the SM Oldroyd-B model in the dashed line. The parameters of these models are shown in Tables I and II, respectively.

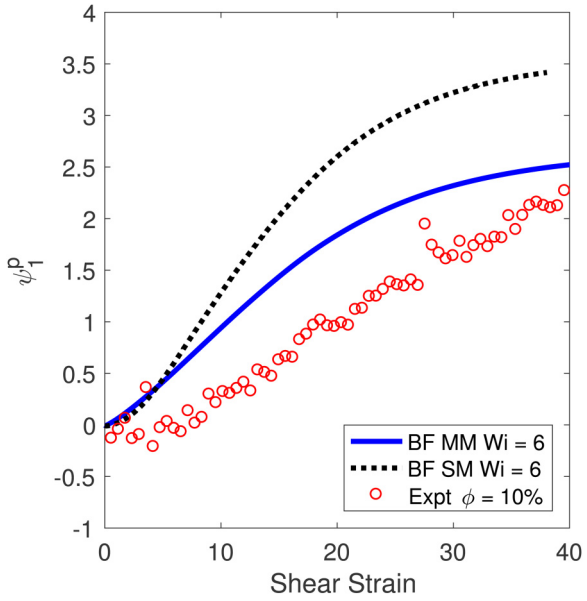

FIG. 22. Comparison of per-particle contribution to first normal stress difference coefficient ψ_1^p of $\phi = 10\%$ suspension in experiments at a shear rate of $6\,s^{-1}$ with single-particle BF simulations at the same largest Wi. The simulation results are shown for the MM and the SM Oldroyd-B models. The parameters of these models are shown in Tables I and II, respectively.

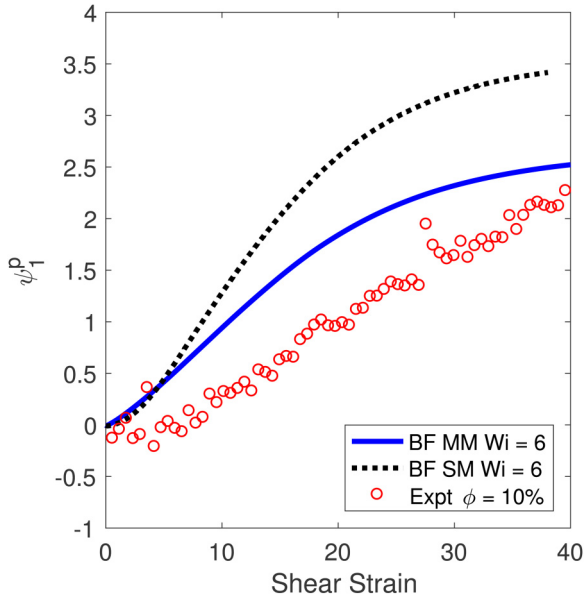

FIG. 24. Comparison of per-particle contribution to the first normal stress difference coefficient of a suspension ψ_1^p from experiments and IB simulations at the shear rate of $6\,s^{-1}$ or largest $Wi = 6$. The BF simulation results are shown in the black solid line in the figure.

values of these suspensions are very close to the suspending fluid at all shear strains as shown in Fig. 20. At a higher shear rate of $6\,s^{-1}$, 10% suspension has a stronger signal in experiments that allows us to compute ψ_1^p values and compare against numerical simulations. The agreement in ψ_1^p values between BF simulations and 10% suspension experimental data is reasonable at $Wi = 6$. The BF simulation result with the MM Oldroyd-B parameters is closer to the experimental data compared to the BF simulation result with SM Oldroyd-B parameters.

Next, we present the direct comparison of the per-particle viscosity between experiments and the IB simulations for nondilute particle suspensions having particle volume fractions $\phi = 2.5\%$, 5%, and 10% at $Wi = 3$ and $Wi = 6$ in Fig. 23. We used the approach that we discussed in Sec. II C for the calculation of per-particle viscosity and per-particle first normal stress difference coefficient in IB simulations. The time-dependent IB simulations provide good quantitative agreement to the experimental per-particle viscosity data at $Wi = 3$, but the steady state values in the simulations are smaller compared to that of the experiments for $\phi = 5\%$ and 10%. Likewise, the IB simulations for $\phi = 2.5\%$ and 5% at $Wi = 6$ show quantitative agreement with transient experimental data except the steady state values are underpredicted for $\phi = 5\%$. The IB simulations for 10% significantly underpredict the per-particle viscosity in experiments at all shear strains. This is perhaps an indicator that we need a finer

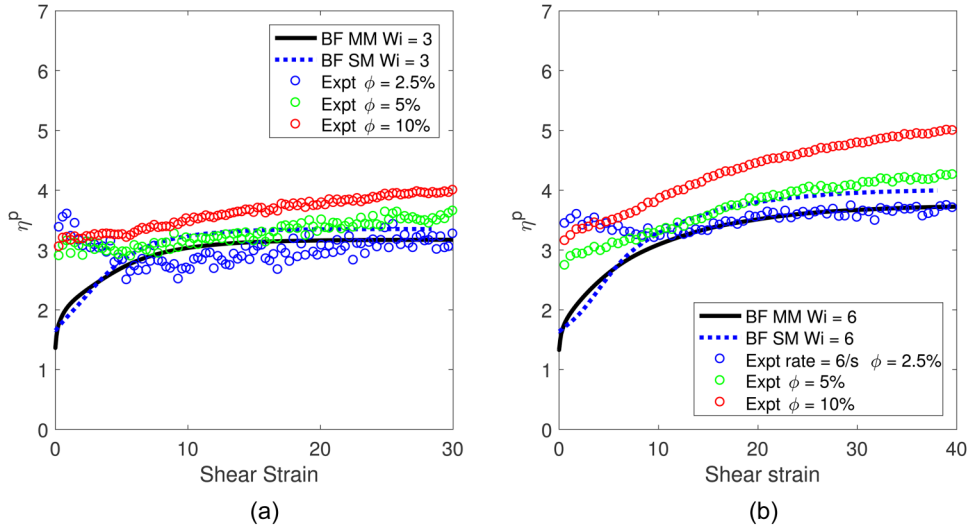

FIG. 23. Comparison of per-particle viscosity η^p from experiments and IB simulations at the shear rate of $3\,s^{-1}$ or largest Wi= 3 (a), and $6\,s^{-1}$ or largest Wi= 6 (b). We superpose the BF simulation results (shown in the black solid line) at the same Wi values.

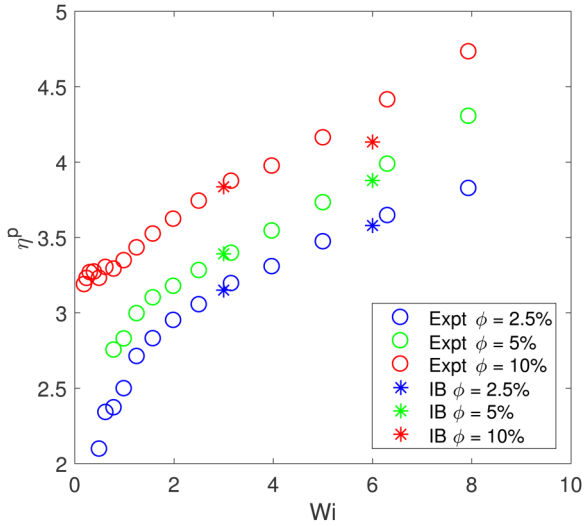

FIG. 25. Comparison of per-particle viscosity from steady shear experiments with steady values from IB simulations for different particle volume fractions.

Eulerian mesh to resolve stresses near the particle surfaces at this high Wi value and particle concentration. This is similar to the situation in previous studies where the Multiple-particle simulations underpredict the thickening in experiments for $\phi \leq 10\%$ in Yang and Shaqfeh [5] or underpredict the steady relative viscosity of viscoelastic particle suspensions ($\phi = 10\%$ and 30%) in experiments at different Wi values in the study by Vázquez *et al.* [7].

Despite the lack of quantitative agreement between the IB simulations and experiments at larger strains and higher ϕ values, the IB simulations show an increase in per-particle viscosity with particle volume fraction ϕ at a given Wi, just as we observe in experiments. To reduce the temporal fluctuations in the average values of the per-particle viscosity, we also performed simulations with 80 spheres in a larger box of sizes $L_1 = 15a, L_2 = 30a$, and $L_3 = 7.5a$ to obtain $\phi = 10\%$. However, we had to use coarser Eulerian and Lagrangian meshes with this large number of particles to manage computation time, but we ensured that the ratio of Lagrangian mesh size to Eulerian mesh size was approximately the same as before. The Eulerian mesh resolution was set to be $h \approx a/6.667$. We present results of this bigger simulation Sec. VI.

We also present the comparison of per-particle first normal stress difference coefficient ψ_1^p from experiments (for 10% suspension) and IB simulations for different particle volume fractions at Wi = 6 in Fig. 24. The IB simulations indicate a weak dependence on ϕ; thus, it can be expected that single-particle BF simulations would do a good job of predicting ψ_1^p in experiments up to 10%. Finally, we present the comparison of the steady state per-particle viscosity from experiments and IB simulation results for different particle volume fractions in Fig. 25. We used the data in Fig. 18(a) to compute the steady state per-particle viscosity in experiments as a function of Wi and used the longest relaxation time of $1\,s^{-1}$ found above to calculate Wi from the imposed shear rate. We find that IB simulations are in close agreement with the experimental data at Wi = 3 for all the three ϕ values considered. At higher Wi = 6, the agreement is quantitative for $\phi = 2.5\%$ and 5%, but the simulations underpredict the steady state value in experiments for 10% suspension as seen in transient shear experiments also. Note the per-particle viscosity values for 5% and 10% suspensions in the steady shear experiments are slightly smaller compared to the steady values obtained from long times in transient shear experiments.

VI. MECHANISM OF INCREASE IN η^p WITH PARTICLE VOLUME FRACTION

In order to understand what causes the increase in per-particle viscosity with particle volume fraction ϕ at a given Wi in transient shear experiments of viscoelastic suspensions, we decompose the per-particle viscosity in the IB simulations into two components—PIFS and stresslet—using the approach discussed above in Sec. II C. We plot the PIFS

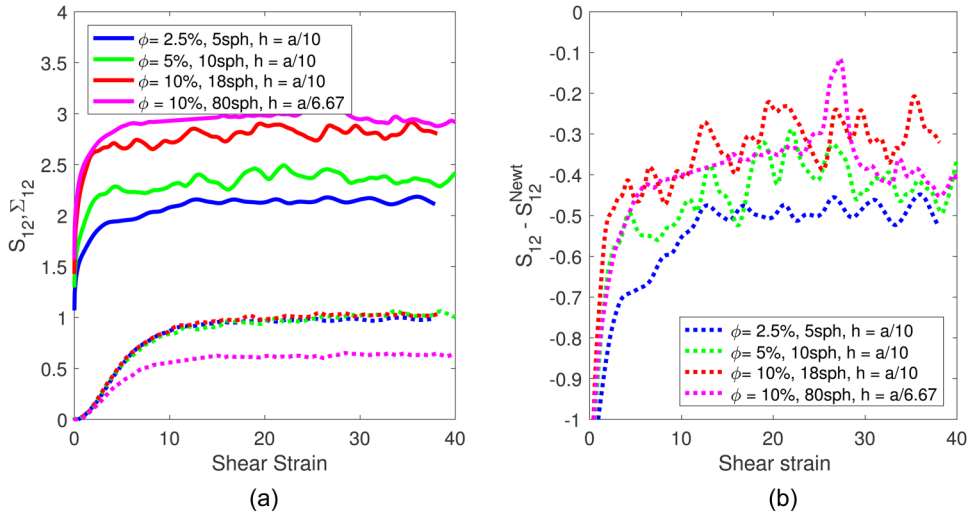

FIG. 26. Decomposition of per-particle viscosity η_{12}^p in IB simulations into PIFS Σ_{12} (dotted lines) and stresslet S_{12} (solid lines) at Wi = 3 (a) and stresslet contribution after Newtonian stresslet is subtracted for different particle volume fractions $\phi = 2.5\%$, 5%, and 10% at Wi = 3 (b). We use Krieger–Dougherty relation for the calculation of Newtonian stresslet in nondilute suspensions that is abbreviated by KD in the figure.

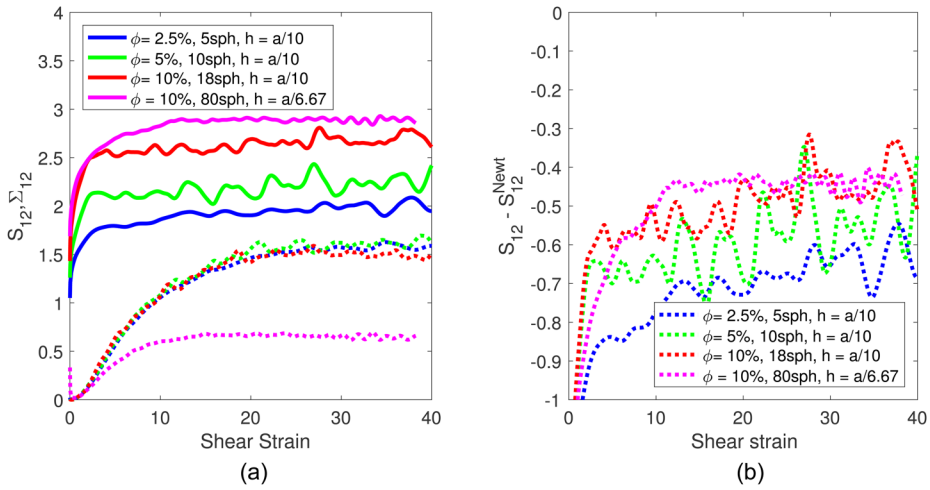

FIG. 27. Decomposition of per-particle viscosity η_{12}^{p} in IB simulations into PIFS Σ_{12} (dotted lines) and stresslet S_{12} (solid lines) at Wi = 6 (a) and stresslet contribution after Newtonian stresslet is subtracted for different particle volume fractions $\phi = 2.5\%$, 5%, and 10% at Wi = 6. We use the Krieger–Dougherty relation for the calculation of Newtonian stresslet in nondilute suspensions that is abbreviated by KD in this figure.

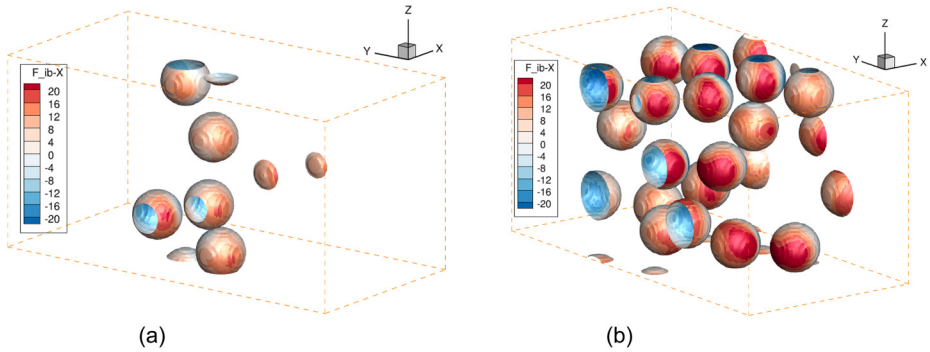

FIG. 28. Surface contours of f_1^{IB} on spheres for $\phi = 2.5\%$ (a) and $\phi = 10\%$ (b) at Wi= 6 in steady state.

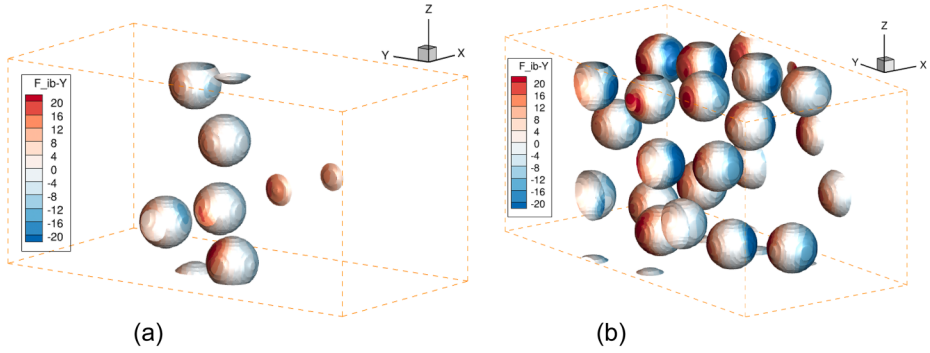

FIG. 29. Surface contours of f_2^{IB} on spheres for $\phi = 2.5\%$ (a) and $\phi = 10\%$ (b) at Wi= 6 in steady state.

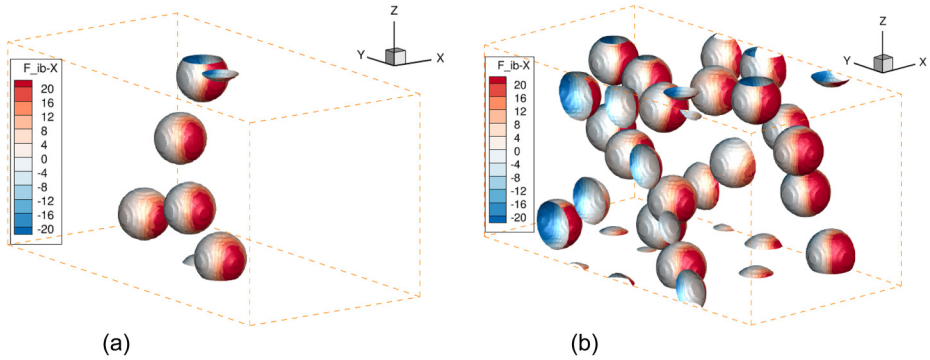

FIG. 30. Surface contours of f_1^{IB} on spheres for $\phi = 2.5\%$ (a) and $\phi = 10\%$ (b) at Wi= 0 in steady state.

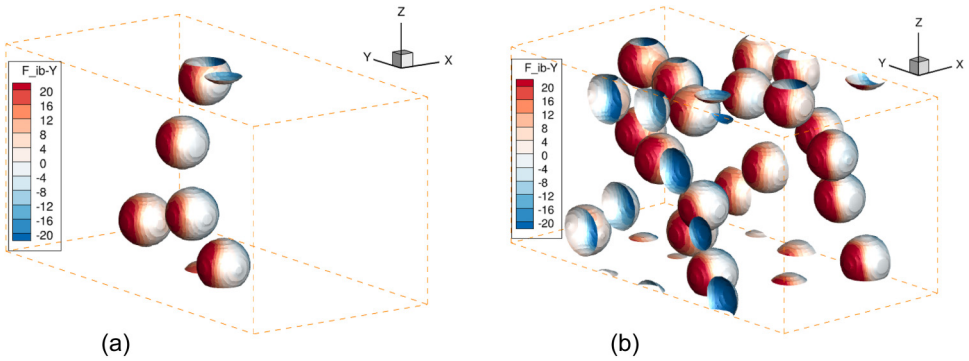

FIG. 31. Surface contours of f_2^{IB} on spheres for $\phi = 2.5\%$ (a) and $\phi = 10\%$ (b) at Wi= 0 in steady state.

and stresslet contributions as a function of shear strain for different ϕ suspensions at Wi = 3 in Fig. 26(a) and find that the PIFS is approximately equal for all suspensions but the stresslet increases with ϕ. This is remarkable as it suggests that particle-particle interactions do not affect the "extra" polymer stress in the fluid phase, i.e., the PIFS, as discussed by Yang and Shaqfeh [5] (for the steady state). This is the case because the regions that contribute most to the PIFS are close to the particle surface where the streamlines form closed trajectories [6]. The particle-particle hydrodynamic interactions cause the stresslet to change with ϕ. We observe the same behavior at higher Wi = 6 in Fig. 27(a). We also plot simulation results for $\phi = 10\%$ with 80 spheres in a bigger computation domain for both Wi values and find that simulating more particles does indeed smooth the temporal fluctuations in the IB simulations, but due to the coarser mesh resolution, the simulations underpredict the PIFS significantly. The simulation results for the stresslet computed using 80 spheres agree with the results calculated on the smaller computation domain.

The steady state stresslet values in Newtonian suspensions increase nonlinearly with ϕ as seen in Fig. 6. Since the numerical values from IB simulations are in excellent agreement with the Kreiger–Dougherty relation, we use this relation to calculate the relative viscosity of Newtonian suspensions at finite particle concentration.

One of the objectives of this study is to determine whether there is a need to simulate multiple particles or it suffices to perform single-particle simulations to study the bulk rheology of nondilute particle suspensions in shear flow. Thus, we need to determine if the per-particle stresslet can be made independent of ϕ, as the PIFS contribution is already independent of ϕ. We know that the Newtonian stresslet contribution depends nonlinearly on ϕ; therefore, we subtract the Newtonian contribution from the per-particle stresslet and determine if the remainder (that we refer to as "elastic" stresslet) is a function of the particle volume fraction. We plot the "elastic" stresslet contribution $S_{12} - S_{12}^{Newt}$ at Wi = 3 in Fig. 26(b) and Wi = 6 in Fig. 27(b) for $\phi = 2.5\%$, 5%, and 10% suspensions. The "elastic" stresslet contribution depends on ϕ (in particular, increases with ϕ) for both values of Wi investigated, which suggests that it is necessary to simulate multiple particles to capture the nonlinear effect of particle-particle hydrodynamic interactions on the bulk rheology of nondilute particle suspensions in viscoelastic fluids. We also present the elastic stresslet contribution from the simulation of 80 spheres ($\phi = 10\%$) in a bigger computation domain at both Wi values. Note that the elastic stresslet values are negative for all ϕ and Wi numbers studied, which simply states that the particle stresslet in elastic suspending fluids is smaller than in Newtonian fluids at the same particle volume fraction.

To help visualize the increase in stresslet values with ϕ, we plot the contours of the IB force density, f_1^{IB} and f_2^{IB}, on the surface of spheres for $\phi = 2.5\%$ and $\phi = 10\%$ at large strains (when the system has reached steady state) and Wi = 6 in Figs. 28 and 29. The IB force density is used in the calculation of stresslet in IB simulations. There are regions on sphere surface where the magnitude of f_1^{IB} and f_2^{IB} is larger for $\phi = 10\%$ compared to $\phi = 2.5\%$ that leads to higher values of "elastic" stresslet for 10% suspension compared to 2.5% suspension in Fig. 27(b). We also show the contours of f_1^{IB} and f_2^{IB} at the same particle volume fractions in Newtonian steady state in Figs. 30 and 31 although the steady distribution of particles is different in the Newtonian case compared to Wi = 6. The Newtonian contours show more regions of large magnitude of f_1^{IB} and f_2^{IB} compared to the Wi = 6 case, which leads to negative values of elastic stresslet for both ϕ values at this Wi = 6. Finally, we want to mention that our simulation results are consistent with the steady findings of Yang *et al.* [13] who show that the thickening of the per-particle viscosity with Wi is due to the increase of PIFS with Wi. We see a similar trend for the PIFS and stresslet in Figs. 26(a) and 27(a), i.e., steady values of PIFS increase with Wi and steady values of stresslet decrease with Wi for all ϕ values.

VII. CONCLUSION

We performed 3D transient simulations of the bulk shear rheology of particle suspensions in Boger fluids for a range of Wi and finite strains and calculated the per-particle extra viscosity of the suspension. We developed a new theory for the time-dependent evolution of average stress in a dilute suspension valid for Wi $\ll 1$ and found good agreement between single-particle dilute simulations and theoretical calculations. To understand the physical mechanism behind the rheology, we categorize the per-particle viscosity calculations as contributions from either PIFS or stresslet. In the dilute limit, the PIFS increases monotonically with shear strain; however, the stresslet

shows a nonmonotonic evolution to steady state at large Wi. This, we believe, is due to the shielding effect in elastic fluids that leads to reduced local surface tractions on the sphere with increasing polymer stretch in the surrounding fluid. The per-particle viscosity, however, shows a monotonic evolution to steady state. We also performed multiple-particle simulations using the IB method to examine the effect of particle-particle hydrodynamic interactions on the per-particle viscosity calculation. Since the solid-fluid interface is not sharp in the IB simulations, we developed and validated a novel method of computing the PIFS and the stresslet in these simulations. The per-particle viscosity and the per-particle contribution to the first normal stress difference coefficient both evolve monotonically to steady state for different Wi and varying particle volume fraction ϕ suspensions. The steady values of per-particle viscosity increase with ϕ, but the per-particle contribution to the primary normal coefficient is independent of ϕ (up to 10% particle volume fraction) at the two Wi values investigated in transient shear IB simulations.

We presented experimental measurements of different ϕ suspensions in a Boger fluid including SAOS, steady shear, and transient shear measurements using cone-and-plate geometry. The transient shear measurements show that it takes longer strains for suspensions to reach steady state with increase in particle loading ϕ and shear rate. These findings reinforce the idea that it is important to study the transient shear rheology of suspensions in viscoelastic fluids where it may take anywhere from 20 to 300 strain units to reach steady state. We also developed a theory for the analytical calculation of η' and G' of different particle volume fraction suspensions in an Oldroyd-B fluid and found excellent agreement with the experimental measurements. We obtained the best four-mode Oldroyd-B parameters for the suspending fluid (by fitting to the SAOS and the stress relaxation data of the fluid) to use in simulations so that a direct comparison can be performed with experiments. We achieved excellent quantitative agreement between experiments and simulations for different ϕ values at $\mathrm{Wi} = 3$ except that the IB simulations underpredict the steady viscosity for a 10% suspension. At higher $\mathrm{Wi} = 6$, the IB simulations underpredict the per-particle viscosity for the 10% suspension at all shear strains and the steady viscosity for a 5% suspension. This suggests that we most probably require a finer Eulerian mesh at higher Wi and higher ϕ values to obtain quantitative agreement with experiments. Nonetheless, IB simulations show an increase in per-particle viscosity with ϕ as observed in experiments.

The per-particle viscosity is decomposed into PIFS and stresslet contributions in the IB simulations to understand what causes the increase in per-particle viscosity with ϕ. We found that the PIFS is approximately equal for different ϕ suspensions, but the stresslet values increase with ϕ. We subtracted the Newtonian stresslet from the per-particle stresslet to obtain "elastic" stresslet contribution and found this to be a function of ϕ as well. The particle-particle hydrodynamic interactions in nondilute suspensions affect the per-particle stresslet and, in turn, the per-particle viscosity. Therefore, one needs to perform multiple-particle simulations to capture the rheology of nondilute viscoelastic suspensions in transient and steady shear flow and compare successfully against experiments.

ACKNOWLEDGMENTS

This work was supported by the National Science Foundation under Grant No. CBET- 1803765. The computations in this paper were performed on the Shepard and Yellowstone cluster at the Stanford HPC Center, supported through awards from the National Science Foundation, DOD HPCMP, and Office of Naval Research. This work also used the Extreme Science and Engineering Discovery Environment (XSEDE) cluster Comet to perform simulations through Allocation Grant No. MCB190002. All the experimental work was performed at the Stanford Nano Shared Facilities (SNSF) that is supported by the National Science Foundation under Award No. ECCS-1542152.

APPENDIX: DERIVATION OF TRANSIENT STRESS AND LINEAR VISCOELASTICITY IN PARTICLE SUSPENSIONS

1. Time dependence of the average stress of a dilute particle suspension in a viscoelastic fluid (Oldroyd-B) through $O(Wi^2)$

A particle is placed in a linear flow that does not change its principal axes but its magnitude can change in time. The flow is started at time $t = 0$ by step increase. The Oldroyd-B model polymer constitutive equation in dimensional form is

$$\lambda\left(\frac{D\tilde{\sigma}_{ij}^{p}}{Dt} - \tilde{\dot{\gamma}}_{ik}\tilde{\sigma}_{kj}^{p} - \tilde{\dot{\gamma}}_{jk}\tilde{\sigma}_{kl}^{p}\right) + \tilde{\sigma}_{ij}^{p} = 2\eta_p\tilde{E}_{ij}, \tag{A1}$$

where the substantial derivative is

$$\frac{D}{Dt} = \frac{\partial}{\partial t} + u_k\frac{\partial}{\partial x_k}, \tag{A2}$$

and the rate of strain tensor is

$$\tilde{\dot{\gamma}}_{ij} = \frac{\partial\tilde{u}_i}{\partial\tilde{x}_j}. \tag{A3}$$

The polymer viscosity is denoted by η_p, and the solvent viscosity is denoted by η_s. The solvent stress in dimensional form is

$$\tilde{\sigma}_{ij}^{s} = -\tilde{p}\delta_{ij} + 2\eta_s\tilde{E}_{ij}. \tag{A4}$$

The momentum balance equation at zero *Re* and the continuity equation is

$$\frac{\partial}{\partial\tilde{x}_k}[\tilde{\sigma}_{ik}^{s} + \tilde{\sigma}_{ik}^{p}] = 0; \qquad \frac{\partial\tilde{u}_p}{\partial\tilde{x}_p} = 0. \tag{A5}$$

The boundary condition on surface of particle is

$$\tilde{u}_i = \tilde{U}_i + \varepsilon_{ijk}\tilde{\Omega}_j\tilde{x}_k, \tag{A6}$$

subject to force-free and torque-free conditions,

$$\int \tilde{\sigma}_{ij} n_j \mathrm{d}A = 0; \qquad \int \varepsilon_{ijk} \tilde{x}_j \tilde{\sigma}_{kl} n_l \mathrm{d}A = 0. \tag{A7}$$

The total stress in fluid phase is given by the sum of solvent stress and polymer stress,

$$\tilde{\sigma}_{ij} = \tilde{\sigma}^s_{ij} + \tilde{\sigma}^p_{ij}. \tag{A8}$$

The far field velocity goes to $\tilde{u}_i \to \langle \tilde{\dot{\gamma}}_{ij} \rangle \tilde{x}_j$ where

$$\langle \cdot \rangle = \frac{1}{V} \int (\cdot) \mathrm{d}V = \frac{1}{V} \left[\int_{V_f} (\cdot) \mathrm{d}V + \int_{V_p} (\cdot) \mathrm{d}V \right]. \tag{A9}$$

and

$$\langle \cdot \rangle_f = \frac{1}{V} \left[\int_{V_f} (\cdot) \mathrm{d}V \right] \tag{A10}$$

The bulk stress in suspension is the sum of stress in fluid phase and particle stresslet,

$$\langle \tilde{\sigma}_{ij} \rangle = \langle \tilde{\sigma}_{ij} \rangle_f + \frac{1}{V} \tilde{S}_{ij}. \tag{A11}$$

The stresslet can be computed as

$$\tilde{S}_{ij} = \int_{A_p} \tilde{x}_j \tilde{\sigma}_{ik} n_k \mathrm{d}A \tag{A12}$$

$$= \frac{1}{2} \int_{A_p} \left[\tilde{x}_j \tilde{\sigma}_{ik} n_k + \tilde{x}_i \tilde{\sigma}_{jk} n_k \right] \mathrm{d}A \tag{A13}$$

$$= \frac{1}{2} \int_{A_p} \left[\tilde{x}_j \tilde{f}_i + \tilde{x}_i \tilde{f}_j \right] \mathrm{d}A. \tag{A14}$$

For Newtonian fluid,

$$\tilde{\sigma}^p_{ij} = 2\eta_p \tilde{E}_{ij}, \tag{A15}$$

$$\langle \tilde{\sigma}_{ij} \rangle_f = -\langle \tilde{p} \rangle_f + 2(\eta_s + \eta_p) \langle \tilde{E}_{ij} \rangle. \tag{A16}$$

Additionally, we will need the reciprocal theorem for a non-Newtonian fluid (denoted by superscript NN) with a Newtonian part (denoted by superscript N) to the stress,

$$\tilde{\sigma}_{ij} = \tilde{\sigma}^N_{ij} + \tilde{\sigma}^{NN}_{ij}. \tag{A17}$$

The surface traction is defined as

$$\tilde{f}_i = \tilde{\sigma}_{ij} n_j \Big|_{\text{surface of particle}}. \tag{A18}$$

Then,

$$\int_{A_p} \tilde{u}^*_i \tilde{f}_i \mathrm{d}A - \int_{A_p} \tilde{u}_i \tilde{f}^*_i \mathrm{d}A = \int_{V_f} \tilde{\dot{\gamma}}^*_{ij} \tilde{\sigma}^{NN}_{ij} \mathrm{d}V, \tag{A19}$$

where $(\cdot)^*$ is the reference solution to the Stokes equations. Making variables nondimensional,

$$\begin{aligned} \tau &= \frac{t}{\lambda}, \qquad & \sigma^p_{ij} &= \frac{\tilde{\sigma}^p_{ij}}{\eta_p \dot{\gamma}}, \qquad & \dot{\gamma}_{ij} &= \frac{\tilde{\dot{\gamma}}_{ij}}{\dot{\gamma}}, \qquad & u_i &= \frac{\tilde{u}_i}{\dot{\gamma} a}, \\ x_i &= \frac{\tilde{x}_i}{a}, \qquad & \sigma_{ij} &= \frac{\tilde{\sigma}_{ij}}{(\eta_s + \eta_p)\dot{\gamma}} = \frac{\tilde{\sigma}_{ij}}{\eta_T \dot{\gamma}}, \qquad & \beta &= \frac{\eta_s}{\eta_T}. \end{aligned} \tag{A20}$$

Then, in dimensionless terms,

$$\frac{\partial \sigma^p_{ij}}{\partial \tau} + Wi \left(u_k \frac{\partial \sigma^p_{ij}}{\partial x_k} - \dot{\gamma}_{ik} \sigma^p_{kj} - \dot{\gamma}_{jk} \sigma^p_{ki} \right) + \sigma^p_{ij} = 2E_{ij}. \tag{A21}$$

$$\sigma^s_{ij} = -p\delta_{ij} + 2E_{ij}. \tag{A22}$$

$$\sigma_{ij} = \beta \sigma^s_{ij} + (1-\beta)\sigma^p_{ij}. \tag{A23}$$

$$\frac{\partial}{\partial x_k} [\beta \sigma^s_{ik} + (1-\beta)\sigma^p_{ik}] = 0. \tag{A24}$$

and

$$\langle \sigma_{ij} \rangle = \langle \beta \sigma^s_{ij} + (1-\beta)\sigma^p_{ij} \rangle_f + \frac{a^3}{V} S_{ij}. \tag{A25}$$

where a is sphere radius and $\dot{\gamma}$ is some measure of average $\langle \dot{\gamma}_{ij} \rangle$. Now, we expand the equations in a power series in Wi noting that

$$\langle \dot{\gamma}_{ij} \rangle = \Gamma_{ij} H(\tau). \tag{A26}$$

In the above equation, Γ_{ij} is constant and $H(\tau)$ is a Heaviside step function. According to regular perturbation theory,

$$\sigma^p_{ij} = \sigma^{p(0)}_{ij} + Wi\sigma^{p(1)}_{ij} + Wi^2 \sigma^{p(2)}_{ij} + \ldots, \tag{A27}$$

$$\sigma^s_{ij} = \sigma^{s(0)}_{ij} + Wi\sigma^{s(1)}_{ij} + Wi^2 \sigma^{s(2)}_{ij} + \ldots, \tag{A28}$$

$$u_i = u^{(0)}_i + Wiu^{(1)}_i + Wi^2 u^{(2)}_i + \ldots, \tag{A29}$$

$$\sigma_{ij} = \sigma^{(0)}_{ij} + Wi\sigma^{(1)}_{ij} + Wi^2 \sigma^{(2)}_{ij} + \ldots, \tag{A30}$$

$$p = p^{(0)} + Wip^{(1)} + Wi^2 p^{(2)} + \ldots, \tag{A31}$$

$$E_{ij} = E^{(0)}_{ij} + WiE^{(1)}_{ij} + Wi^2 E^{(2)}_{ij} + \ldots. \tag{A32}$$

Solving at $O(Wi^{(0)})$ gives

$$\sigma_{ij}^{p(0)} = 2\int_0^\tau exp(-(\tau-\tau'))E_{ij}^{(0)}(x_i,\tau')\partial\tau', \tag{A33}$$

and this stress term is quasi-Newtonian. The driving force for the flow is $\dot{\gamma}_{ij} \to \Gamma_{ij}H(\tau)$ in the far field. Moreover, the Newtonian flow does not depend on viscosity, and thus we assume

$$u_i^{(0)} = U_i^{(0)}(x_i)H(\tau) \tag{A34}$$

and

$$E_{ij}^{(0)} = e_{ij}^{(0)}(x_i)H(\tau), \tag{A35}$$

and define

$$L\{H(\tau)\} = \int_0^\tau \exp(-(\tau-\tau'))H(\tau')\partial\tau' = 1-\exp(-\tau). \tag{A36}$$

We obtain

$$\sigma_{ij}^{p(0)} = 2e_{ij}^{(0)}(x_i)L\{H(\tau)\}. \tag{A37}$$

Substituting polymer stress in momentum balance equation gives

$$-\beta\frac{\partial p^{(0)}}{\partial x_i} + \beta\nabla^2 U_i^{(0)}H(\tau) + (1-\beta)\nabla^2 U_i^{(0)}L\{H(\tau)\} = 0. \tag{A38}$$

We then have

$$p^{(0)} = P^{(0)}f(\tau), \tag{A39}$$

where

$$f(\tau) = H(\tau) + \frac{1-\beta}{\beta}L\{H(\tau)\} \tag{A40}$$

and

$$-\frac{\partial P^{(0)}}{\partial x_i} + \nabla^2 U_i^{(0)} = 0; \quad \frac{\partial U_i^{(0)}}{\partial x_i} = 0. \tag{A41}$$

The above equations are steady Stokes flow equations for the Newtonian fluid. Thus,

$$U_i^{(0)} = \Gamma_{ij}x_j - 5/2\text{sym}(\Gamma_{jk})\frac{x_ix_jx_k}{r^5} + 5/2\text{sym}(\Gamma_{jk})\left(\frac{x_ix_jx_k}{r^7} - \frac{x_j\delta_{ik}+x_k\delta_{ij}}{5r^5}\right), \tag{A42}$$

where

$$\text{sym}(\Gamma_{ij}) = 1/2\left(\Gamma_{ij}+\Gamma_{ji}\right) \tag{A43}$$

and

$$\dot{\gamma}_{ij}^{(0)} = \frac{\partial U_i^{(0)}}{\partial x_j}H(\tau) = g_{ij}^{(0)}H(\tau); \quad \Omega_i^{(0)} = \frac{\omega_i^{(0)}}{2}H(\tau). \tag{A44}$$

Here, $\omega_i^{(0)}$ is the vorticity associated with Γ_{ij}. The average stress at $O(Wi^{(0)})$ is given according to

$$\langle\sigma_{ij}^{(0)}\rangle_f = -\langle p^{(0)}\rangle_f\delta_{ij}f(\tau) + 2\beta\text{sym}\Gamma_{ij}H(\tau) + 2(1-\beta)\text{sym}\Gamma_{ij}L\{H(\tau)\}, \tag{A45}$$

$$\frac{a^3}{V}S_{ij} = \phi\left(5\beta\text{sym}(\Gamma_{ij})H(\tau) + 5(1-\beta)\text{sym}(\Gamma_{ij})L\{H(\tau)\}\right). \tag{A46}$$

Thus we obtain $\langle\sigma_{ij}^{(0)}\rangle$ according to Eq. (A25) as

$$\langle\sigma_{ij}^{(0)}\rangle = \text{Isotropic Terms} + 2\beta E_{ij}H(\tau) + 2(1-\beta)E_{ij}(1-\exp(-\tau)) + 5\phi\beta E_{ij}H(\tau) + 5\phi(1-\beta)E_{ij}(1-\exp(-\tau)). \tag{A47}$$

At next order $O(Wi^{(1)})$, Eq. (A21) gives

$$\frac{\partial\sigma_{ij}^{p(1)}}{\partial t} + \sigma_{ij}^{p(1)} = 2E_{ij}^{(1)} + S_{ij}^{p(0)}H(\tau)L\{H(\tau)\}, \tag{A48}$$

where

$$S_{ij}^{p(0)} = -2U_k^{(0)}\frac{\partial e_{ij}^{(0)}}{\partial x_k} + 2g_{ik}^{(0)}e_{kj}^{(0)} + 2g_{jk}^{(0)}e_{ki}^{(0)}. \tag{A49}$$

We assume

$$u_i^{(1)} = U_i^{(1)}(x_i)H^{(1)}(\tau), \tag{A50a}$$

$$E_{ij}^{(1)} = e_{ij}^{(1)}(x_i)H^{(1)}(\tau), \tag{A50b}$$

where $H^{(1)}(\tau)$ is to be determined. Solving for $\sigma_{ij}^{p(1)}$ with initial condition $\sigma_{ij}^{p(1)}(\tau=0)$ gives

$$\sigma_{ij}^{p(1)} = 2e_{ij}^{(1)}(x_i)L\{H^{(1)}(\tau)\} + S_{ij}^{p(0)}L\{H(\tau)L\{H(\tau)\}\}. \tag{A51}$$

The integration gives

$$L\{H(\tau)L\{H(\tau)\}\} = 1 - \exp(-\tau) - \tau\exp(-\tau). \tag{A52}$$

Assuming $p^{(1)} = P^{(1)}f^{(1)}(\tau)$, the conservation of momentum

gives

$$-\beta\frac{\partial P^{(1)}}{\partial x_i}f^{(1)}(\tau)+\beta\Delta^2U_i^{(1)}H^{(1)}(\tau)+(1-\beta)\Delta^2U_i^{(1)}L\{H^{(1)}(\tau)\}+(1-\beta)\left[\frac{\partial S_{ij}^{p(0)}}{\partial x_j}\right]L\{H(\tau)L\{H(\tau)\}\}=0. \tag{A53}$$

By balancing terms we get

$$H^{(1)}=\frac{1-\beta}{\beta}L_\beta[H(\tau)L\{H(\tau)\}], \tag{A54}$$

where L_β is defined as

$$L_\beta(\phi(\tau))=\int_0^\tau \exp(-\left(\frac{\tau-\tau'}{\beta}\right)\phi(\tau')d\tau' \tag{A55}$$

and

$$f^{(1)}=\frac{1-\beta}{\beta}L\{H(\tau)L\{H(\tau)\}\}. \tag{A56}$$

With this solution, the entire problem goes back to the steady problem at $O(Wi^{(1)})$. The momentum conservation gives

$$-\frac{\partial P^{(1)}}{\partial x_i}+\nabla^2U_i^{(1)}+\frac{\partial S_{ij}^{p(0)}}{\partial x_j}=0, \tag{A57}$$

with $u_i^{(1)}\to 0$ as $r\to\infty$. The velocity on the particle surface is given by

$$u_i^{(1)}=U_i^{(1)}+\varepsilon_{ijk}\omega_j^{(1)}x_k|_{r=1}, \tag{A58}$$

where $\Omega_i^{(1)}=\omega_i^{(1)}H^{(1)}(\tau)$ and $u_i^{(1)}=U_i^{(1)}H^{(1)}(\tau)$. Note that $U_i^{(1)}=0$ by symmetry. It is difficult to find $U_i^{(1)}$ or $e_{ij}^{(1)}$, but we do not have to calculate these quantities to get the average stress. We know $\langle e_{ij}^{(1)}\rangle_f=0$; therefore, we obtain

$$\langle\sigma_{ij}^{(1)}\rangle_f=\text{Isotropic term}+(1-\beta)\langle S_{ij}^{p(0)}\rangle_f L\{H(\tau)L\{H(\tau)\}\}. \tag{A59}$$

We use the reciprocal theorem in Eq. (A19) with the reference field for disturbance flow as extensional flow past a sphere and we obtain stresslet according to

$$\frac{a^3}{V}S_{ij}=-(1-\beta)\langle M_{mlij}S_{ml}^{p(0)}\rangle_f L\{H(\tau)L\{H(\tau)\}\}, \tag{A60}$$

where $\dot\gamma_{ij}^*=E_{ml}^*M_{ijml}$ where $(\cdot)^*$ is the reference solution for extensional flow in this case. We note that the time-dependent functional form in Eqs. (A59) and (A60) is identical but the coefficients are different. These coefficients have been computed in the study [16]. Thus, we obtain bulk stress at this order as

$$\langle\sigma_{ij}^{(1)}\rangle=(1-\beta)\phi A_{ij}(1-\exp(-\tau)-\tau\exp(-\tau)), \tag{A61}$$

with the coefficients lumped into A_{ij}. There is no correction to shear stress in shear flow at this order as shown by Einarsson *et al.* [16]. We move to next order $O(Wi^{(2)})$,

$$\frac{\partial\sigma_{ij}^{p(2)}}{\partial t}+\sigma_{ij}^{p(2)}=-U_k^{(0)}\frac{\partial\sigma_{ij}^{p(1)}}{\partial x_k}+\dot\gamma_{ik}^{(0)}\sigma_{kj}^{p(1)}+\dot\gamma_{jk}^{(0)}\sigma_{ki}^{p(1)}-U_k^{(1)}\frac{\partial\sigma_{ij}^{p(0)}}{\partial x_k}+\dot\gamma_{ik}^{(1)}\sigma_{kj}^{p(0)}+\dot\gamma_{jk}^{(1)}\sigma_{ki}^{p(0)}+2E_{ij}^{(0)}. \tag{A62}$$

The first three terms on the rhs of above equation can be called "forcing terms 1" and the next three terms on rhs can be called "forcing terms 2." The solvent stress can be written as

$$\sigma_{ij}^{s(2)}=-p^{(2)}\delta_{ij}+2E_{ij}^{(2)}, \tag{A63}$$

and the total stress would be

$$\sigma_{ij}^{(2)}=\beta\sigma_{ij}^{s(2)}+(1-\beta)\sigma_{ij}^{p(2)}. \tag{A64}$$

The momentum balance and continuity equations at this order give

$$\frac{\partial\sigma_{ik}^{(2)}}{\partial x_k}=0;\qquad\frac{\partial U_i^{(2)}}{\partial x_i}=0, \tag{A65}$$

with $U_i^{(2)}\to 0$ as $r\to\infty$ and $U_i^{(2)}=\varepsilon_{ikl}\omega_k^{(2)}x_l$ at $r=a$ plus no force and no torque conditions. We substitute the time-dependent functional form of different variables in above Eq. (A62) and find that there are three different forcing terms,

$$\frac{\partial\sigma_{ij}^{p(2)}}{\partial t}+\sigma_{ij}^{p(2)}=S_{ij}^{00}H(\tau)L\{H(\tau)L\{H(\tau)\}\}+S_{ij}^{01}H(\tau)L\{L_\beta\{H(\tau)L\{H(\tau)\}\}\}+S_{ij}^{10}L_\beta\{H(\tau)L\{H(\tau)\}\}L\{H(\tau)\}+2E_{ij}^{(2)}, \tag{A66}$$

where

$$S_{ij}^{00}=-U_k^{(0)}\frac{\partial S_{ij}^{p(0)}}{\partial x_k}+g_{ik}^{(0)}S_{kj}^{p(0)}+g_{jk}^{(0)}S_{ki}^{p(0)}, \tag{A67a}$$

$$S_{ij}^{01}=\left[-2U_k^{(0)}\frac{\partial e_{ij}^{(1)}}{\partial x_k}+2g_{ik}^{(0)}e_{kj}^{(1)}+2g_{jk}^{(0)}e_{ki}^{(1)}\right]\frac{1-\beta}{\beta}, \tag{A67b}$$

$$S_{ij}^{10}=\left[-2U_k^{(1)}\frac{\partial e_{ij}^{(0)}}{\partial x_k}+2g_{ik}^{(1)}e_{kj}^{(0)}+2g_{jk}^{(1)}e_{ki}^{(0)}\right]\frac{1-\beta}{\beta}, \tag{A67c}$$

$$E_{ij}^{(2)} = e_{ij}^{(2)} H^{(2)}(\tau), \tag{A67d}$$

where $H^{(2)}(\tau)$ is not known. It follows then,

$$\begin{aligned}\sigma_{ij}^{p(2)} = {} & S_{ij}^{00} L\{H(\tau)L\{H(\tau)L\{H(\tau)\}\}\} \\ & + S_{ij}^{01} L\{H(\tau)L\{L_\beta\{H(\tau)L\{H(\tau)\}\}\}\} \\ & + S_{ij}^{10} L\{L_\beta\{H(\tau)L\{H(\tau)\}\}L\{H(\tau)\}\} + 2e_{ij}^{(2)} L\{H^{(2)}(\tau)\}.\end{aligned} \tag{A68}$$

We evaluate the Laplace of different terms by performing integration. Then,

$$\begin{aligned}\langle \sigma_{ij}^{p(2)} \rangle_f = {} & \langle S_{ij}^{00} \rangle_f L\{H(\tau)L\{H(\tau)L\{H(\tau)\}\}\} \\ & + \langle S_{ij}^{01} \rangle_f L\{H(\tau)L\{L_\beta\{H(\tau)L\{H(\tau)\}\}\}\} \\ & + \langle S_{ij}^{10} \rangle_f L\{L_\beta\{H(\tau)L\{H(\tau)\}\}L\{H(\tau)\}\},\end{aligned} \tag{A69}$$

since $\langle e_{ij}^{(2)} \rangle_f = 0$. The stresslet has the same time-dependent form as shown in Eq. (A69) with different tensor multipliers as was the case earlier. The bulk stress at this order is given by

$$\begin{aligned}\langle \sigma_{ij}^{(2)} \rangle = {} & B_{ij}\phi\left[1 - \exp(-\tau) - \tau\exp(-\tau) - \frac{\tau^2}{2}\exp(-\tau)\right] \\ & + C_{ij}\phi\left[\beta(1 - \exp(-\tau) - \tau\exp(-\tau)) - \frac{\beta}{2(1-\beta)}\tau^2\exp(-\tau) + \frac{\beta^3}{(1-\beta)^2}\tau\exp(-\tau)\right] \\ & + C_{ij}\phi\left[-\frac{\beta^4}{(1-\beta)^3}(\exp(-\tau) - \exp(-\tau/\beta))\right] \\ & + D_{ij}\phi\left[\beta(1 - \exp(-\tau) - \tau\exp(-\tau)) - \frac{\beta^3}{(1-\beta)^2}(\exp(-\tau/\beta) - \exp(-\tau))\right] \\ & + D_{ij}\phi\left[-\frac{\beta^3}{(1-\beta)}\left(\exp(-\tau) - \exp\left(-\frac{1+\beta}{\beta}\tau\right)\right)\right] \\ & + D_{ij}\phi\left[-\frac{\beta}{(1-\beta)}(\tau\exp(-\tau) - \exp(-\tau) + \exp(-2\tau))\right],\end{aligned} \tag{A70}$$

We find coefficients by fitting to numerical simulations at this order.

2. Theory for linear viscoelasticity of suspensions in Oldroyd-B fluid

We start with dimensional Oldroyd-B polymer constitutive equation as shown in Eq. (A1). Linear response theory means Wi $\ll 1$ at all scales such that we can discard all nonlinear terms in velocity at the particle or macroscale subject to the condition that the time it takes to flow a microlength is still $\dot{\gamma}^{-1}$. Thus, we obtain

$$\lambda \frac{\partial \sigma_{ij}^p}{\partial t} + \sigma_{ij}^p = 2\eta_p E_{ij}. \tag{A71}$$

Transforming $\psi = \hat{\psi}\exp(i\omega t)$ as we are seeking periodic solution. The above differential equation becomes the algebraic equation

$$\lambda i\omega \hat{\sigma_{ij}^p} + \hat{\sigma}_{ij}^p = 2\eta_p \hat{E}_{ij}, \tag{A72}$$

or

$$\hat{\sigma}_{ij}^p = \frac{2\eta_p}{\lambda i\omega + 1}\hat{E}_{ij}. \tag{A73}$$

The above equation says that the polymer stress is a convolution of the rate of strain in time at every point in space, with the convolution time scaling on λ. This means that the fluid is quasi-Newtonian. Since $\sigma_{ij}^f = 2\eta_s E_{ij}$ or

$$\hat{\sigma}_{ij}^f = 2\eta_s \hat{E}_{ij}, \tag{A74}$$

the total stress is obtained using

$$\hat{\sigma}_{ij}^{total} = -\hat{p}\delta_{ij} + \left[2\eta_s + \frac{2\eta_p}{i\lambda\omega + 1}\right]\hat{E}_{ij}, \tag{A75}$$

and the deviatoric component of total stress tensor is

$$\mathrm{dev}(\hat{\sigma}_{ij}^{total}) = \left[2\eta_s + \frac{2\eta_p}{i\lambda\omega + 1}\right]\hat{E}_{ij}. \tag{A76}$$

The volume average of the deviatoric component of total stress tensor is related to stress in the fluid phase and average

of stresslets as

$$\langle \mathrm{dev}(\hat{\sigma}_{ij}^{total}) \rangle = \langle \hat{\sigma}_{ij} \rangle_f + \langle S_{ij} \rangle, \tag{A77}$$

$$\langle \hat{\sigma}_{ij} \rangle_f = \left[2\eta_s + \frac{2\eta_p}{i\lambda\omega + 1} \right] \langle \hat{E}_{ij} \rangle. \tag{A78}$$

The average of stresslets is computed as

$$\begin{aligned} \langle S_{ij} \rangle &= \frac{1}{V} \left(\int_{A_p} S_{ij} \right) \\ &= \left[2\eta_s + \frac{2\eta_p}{i\lambda\omega + 1} \right] \langle \hat{E}_{ij} \rangle f(\phi), \end{aligned} \tag{A79}$$

where A_p is the area of all particles and $f(\phi)$ is the extra viscosity function for a Newtonian fluid at zero Re including all hydrodynamic interactions, for example, $f(\phi) = 5/2\phi$ for $\phi \ll 1$. Putting this together,

$$\langle \mathrm{dev}(\hat{\sigma}_{ij}^{total}) \rangle = \left[2\eta_s + \frac{2\eta_p}{i\lambda\omega + 1} \right] \langle \hat{E}_{ij} \rangle (1 + f(\phi)) \tag{A80}$$

or

$$\langle \mathrm{dev}(\sigma_{ij}^{total}) \rangle = \left[2\eta_s + \frac{2\eta_p}{i\lambda\omega + 1} \right] \langle E_{ij} \rangle (1 + f(\phi)), \tag{A81}$$

where $\langle E_{ij} \rangle$ is still complex and for oscillatory flow,

$$\begin{aligned} \langle E_{ij} \rangle &= \langle \hat{E}_{ij} \rangle \exp(i\omega t) \\ &= \frac{\dot{\gamma}}{2} (\delta_{i1}\delta_{j2} + \delta_{j1}\delta_{i1}) \exp(i\omega t). \end{aligned} \tag{A82}$$

Thus, we obtain

$$\begin{aligned} \langle \sigma_{12}^{total} \rangle = &\left(\eta_s + \eta_p \left[\frac{1 - i\omega\lambda}{1 + (\lambda\omega)^2} \right] \right) (1 \\ &+ f(\phi)) \dot{\gamma} \exp(i\omega t.) \end{aligned} \tag{A83}$$

We obtain expressions for G' and G'' from the real and imaginary parts of Eq. (A83),

$$G' = \frac{\eta_p \lambda \omega^2}{1 + (\lambda\omega)^2} [1 + f(\phi)], \tag{A84}$$

$$G' = \eta_s \omega [1 + f(\phi)] + \frac{\eta_p \omega}{1 + (\lambda\omega)^2} [1 + f(\phi)]. \tag{A85}$$

We apply this for each mode in an MM model and then we sum the contributions to get the results of Eqs. (40) and (41) in the text.

REFERENCES

[1] Chan, D., and R. Powell, "Rheology of suspensions of spherical particles in a newtonian and a non-newtonian fluid," J. Non-Newtonian Fluid Mech. **15**, 165–179 (1984).

[2] Gadala-Maria, F., and A. Acrivos, "Shear-induced structure in a concentrated suspension of solid spheres," J. Rheol. **24**, 799–814 (1980).

[3] James, D. F., "Boger fluids," Annu. Rev. Fluid Mech. **41**, 129–142 (2009).

[4] Dai, S.-C., F. Qi, and R. I. Tanner, "Viscometric functions of concentrated non-colloidal suspensions of spheres in a viscoelastic matrix," J. Rheol. **58**, 183–198 (2014).

[5] Yang, M., and E. S. Shaqfeh, "Mechanism of shear thickening in suspensions of rigid spheres in boger fluids. Part II: Suspensions at finite concentration," J. Rheol. **62**, 1379–1396 (2018).

[6] Yang, M., and E. S. Shaqfeh, "Mechanism of shear thickening in suspensions of rigid spheres in boger fluids. Part I: Dilute suspensions," J. Rheol. **62**, 1363–1377 (2018).

[7] Vázquez-Quesada, A., P. Español, R. I. Tanner, and M. Ellero, "Shear thickening of a non-colloidal suspension with a viscoelastic matrix," J. Fluid Mech. **880**, 1070–1094 (2019).

[8] Zarraga, I. E., D. A. Hill, and D. T. Leighton, Jr., "Normal stresses and free surface deformation in concentrated suspensions of noncolloidal spheres in a viscoelastic fluid," J. Rheol. **45**, 1065–1084 (2001).

[9] Scirocco, R., J. Vermant, and J. Mewis, "Shear thickening in filled Boger fluids," J. Rheol. **49**, 551–567 (2005).

[10] Hwang, W. R., M. A. Hulsen, and H. E. Meijer, "Direct simulations of particle suspensions in a viscoelastic fluid in sliding bi-periodic frames," J. Non-Newtonian Fluid Mech. **121**, 15–33 (2004).

[11] Hwang, W., M. Hulsen, H. Meijer, and T. Kwon, "Direct numerical simulations of suspensions of spherical particles in a viscoelastic fluid in sliding tri-periodic domains," in *Proceedings of the 14th International Congress on Rheology, Seoul*, Korea, August 22–27 (The Korean Society of Rheology, Seoul, 2004).

[12] d'Avino, G., F. Greco, M. Hulsen, and P. Maffettone, "Rheology of viscoelastic suspensions of spheres under small and large amplitude oscillatory shear by numerical simulations," J. Rheol. **57**, 813–839 (2013).

[13] Yang, M., S. Krishnan, and E. S. Shaqfeh, "Numerical simulations of the rheology of suspensions of rigid spheres at low volume fraction in a viscoelastic fluid under shear," J. Non-Newtonian Fluid Mech. **233**, 181–197 (2016).

[14] Krishnan, S., E. Shaqfeh, and G. Iaccarino, ""Immersed boundary methods for viscoelastic particulate flows," APS Division of Fluid Dynamics, Abstract A40.001 (2015).

[15] Krishnan, S., E. S. Shaqfeh, and G. Iaccarino, "Fully resolved viscoelastic particulate simulations using unstructured grids," J. Comput. Phys. **338**, 313–338 (2017).

[16] Einarsson, J., M. Yang, and E. S. Shaqfeh, "Einstein viscosity with fluid elasticity," Phys. Rev. Fluids **3**, 013301 (2018).

[17] Castillo, A., W. L. Murch, J. Einarsson, B. Mena, E. S. Shaqfeh, and R. Zenit, "Drag coefficient for a sedimenting and rotating sphere in a viscoelastic fluid," Phys. Rev. Fluids **4**, 063302 (2019).

[18] Zhang, A., W. L. Murch, J. Einarsson, and E. S. Shaqfeh, "Lift and drag force on a spherical particle in a viscoelastic shear flow," J. Non-Newtonian Fluid Mech. **280**, 104279 (2020).

[19] Mittal, R., and G. Iaccarino, "Immersed boundary methods," Annu. Rev. Fluid Mech. **37**, 239–261 (2005).

[20] Einarsson, J., M. Yang, and E. S. G. Shaqfeh, "Einstein viscosity with fluid elasticity," Phys. Rev. Fluids **3**, 013301 (2018).

[21] Krieger, I. M., and T. J. Dougherty, "A mechanism for non-newtonian flow in suspensions of rigid spheres," Trans. Soc. Rheol. **3**, 137–152 (1959).

[22] Batchelor, G., and J. Green, "The determination of the bulk stress in a suspension of spherical particles to order c^2," J. Fluid Mech. **56**, 401–427 (1972).

[23] Glowinski, R., T.-W. Pan, T. I. Hesla, D. D. Joseph, and J. Periaux, "A fictitious domain approach to the direct numerical simulation of incompressible viscous flow past moving rigid bodies: Application to particulate flow," J. Comput. Phys. **169**, 363–426 (2001).

[24] Sridhar, T., "An overview of the project M1," J. Non-Newtonian Fluid Mech. **35**, 85–92 (1990).

[25] Müller, A., J. Odell, and J. Tatham, "Stagnation-point extensional flow behaviour of M1," J. Non-Newtonian Fluid Mech. **35**, 231–250 (1990).